

PREPARED FOR SUBMISSION

Light Rings, Accretion Disks and Shadows of Hayward Boson Stars in asymptotically AdS Spacetime

Zhen-Hua Zhao^{a,*}, Yi-Ning Gu^a, Shu-Cong Liu^b, Zi-Qian Liu^a, Yong-Qing Wang^{b,*}

^a*Department of Applied Physics, Shandong University of Science and Technology, Qingdao 266590, China*

^b*Lanzhou Center for Theoretical Physics, School of Physical Science and Technology, Lanzhou University, Lanzhou 730000, China*

E-mail: zhaozh78@sdust.edu.cn, *corresponding author,
yqwang@lzu.edu.cn, *corresponding author

ABSTRACT:

In this paper, we employ numerical methods to investigate the fundamental properties of Hayward boson stars and the optical appearance of their accretion disks in asymptotically anti-de Sitter (AdS) spacetime. Our results show that variations in the negative cosmological constant significantly affect the relationship between ADM mass and frequency, the critical magnetic monopole charge, the size of the photon ring, and the kinematic characteristics of particles at the innermost stable circular orbit (ISCO). Through ray-tracing studies of the accretion disk's appearance, we find that for non-frozen boson stars, the absence of an event horizon leads to multiple photon rings appearing within the central shadow region. In contrast, for frozen boson stars, the presence of a critical event horizon causes their images to resemble those of Schwarzschild black holes, with no additional photon rings appearing within the shadow region. Furthermore, the negative cosmological constant significantly alters the image structure: a smaller ISCO radius leads to photon rings being obscured at specific viewing angles, preventing their appearance within the shadow region.

Contents

1	Introduction	1
2	Introduction to the Model	2
3	Numerical scheme	4
4	Numerical results	4
4.1	ADM Mass	5
4.2	Frozen States and Critical Horizon	8
4.3	Light Rings	10
4.4	Accretion Disk and Shadows	13
5	Conclusion	22
6	Acknowledgment	23

1 Introduction

The general theory of relativity, proposed by Einstein in 1916 [1], has been remarkably successful in describing gravitational phenomena, especially in extreme conditions such as strong gravitational fields. Notable examples include the Schwarzschild black hole [2], Kerr black hole [3] and Kerr–Newman black hole [4]. However, the issue of singularities remains unresolved. Singularities are not a reflection of the real physical world but rather a limitation of existing theories when describing the behavior of matter and spacetime under extreme conditions.

To address the singularity problem, regular black holes are proposed as theoretical models to avoid singularity formation. Early attempts to regularize black hole metrics were made by Shirokov (1948) [5], Duan (1954) [6], Sakharov [7] (1966), and Gliner (1966) [8]. In 1968, Bardeen proposed a widely accepted model of regular black holes [9]. Further in 2006, Hayward introduced another model of regular black holes [10].

However, obtaining exact solutions for regular black holes by solving the Einstein equations remains highly challenging. It was not until 1999 that Ayón-Beato and García [11] proposed the first exact regular black hole solution using nonlinear electrodynamics coupled to general relativity. Subsequently, they derived the exact solution for the Bardeen black hole [12], interpreting it as a magnetic monopole. Further, the exact solution Hayward black hole is obtained by Fan and Wang in 2016 [13].

Building upon the pioneering work of Hawking and Page on black hole thermodynamics in Anti-de Sitter (AdS) spacetime [14], comprehensive investigations have been carried out

in recent years into the thermodynamic properties of the Hayward model in AdS space-time [15–30].

Beyond its thermodynamic aspects, the Hayward model has also drawn considerable attention across multiple frontier research areas, including greybody factor and stability analysis [31], construction of extended hydrodynamic models [32], studies on quantum black hole properties [33], quasinormal modes [34–39], as well as computations and analyses of black hole shadow radii [25, 40].

In addition to regular black holes, boson stars are also ideal compact objects that lack singularities and can mimic black holes in many observational features [41–53]. Studies of boson stars were originally carried out under the assumption of asymptotically flat space-time [54]. In recent years, this framework has been extended to asymptotically anti-de Sitter (AdS) spacetimes with a negative cosmological constant [55–58], and further generalized to other similar models such as Dirac stars [59, 60] and Proca stars [61].

This paper aims to present a analysis of certain fundamental properties of Hayward mini-boson stars in AdS spacetime. Compared to the case with vanishing cosmological constant [62], the presence of a negative cosmological constant significantly affects various features of these boson stars, such as their maximum mass, minimum frequency, frozen state, critical horizon radius, and photon sphere radius. In addition, we further investigate the radius, angular momentum, and energy of particles at the innermost stable circular orbit (ISCO) in the accretion disk, and analyze how the negative cosmological constant influences the observable spectral distribution on the accretion disk.

The organization of this paper is as follows. In Sec. 2, the model discussed is presented. In Sec. 3, the numerical scheme is outlined. In Sec. 4, the numerical results and discussion are presented in four topics. In Sec. 5, some conclusions are presented.

2 Introduction to the Model

This section provides a brief introduction to the theoretical model, which combines the Einstein-nonlinear electrodynamics framework proposed in [13, 15] with a complex scalar field. The natural units ($\hbar = c = 1$) are adopted, and the action is given by:

$$S = \int \sqrt{-g} d^4x \left(\frac{R - 2\Lambda}{4\kappa} + \mathcal{L}^{(1)} + \mathcal{L}^{(2)} \right), \quad (2.1)$$

where $\kappa = 4\pi G$, G is the gravitational constant, and Λ is the cosmological constant. The Lagrangian densities are defined as:

$$\mathcal{L}^{(1)} = -\frac{3}{2s} \frac{(2\hat{q}^2 \hat{\mathcal{F}})^{3/2}}{\left(1 + (2\hat{q}^2 \hat{\mathcal{F}})^{3/4}\right)^2}, \quad (2.2)$$

$$\mathcal{L}^{(2)} = -\nabla_\mu \Phi^* \nabla^\mu \Phi - U(\Phi, \Phi^*), \quad (2.3)$$

where, $\hat{\mathcal{F}} = \frac{1}{4} \hat{F}_{\mu\nu} \hat{F}^{\mu\nu}$, $\hat{F}_{\mu\nu} = \partial_\mu \hat{A}_\nu - \partial_\nu \hat{A}_\mu$, $\hat{A}_\mu = \{0, 0, 0, \hat{q} \cos \theta\}$, $\hat{q} = q\sqrt{G}$, q denotes the magnetic monopole charge, and parameter s is free. It is worth noting that the electromagnetic action (2.2) used in this paper is similar to that in [12], but differs from the one adopted in [15].

The self-interaction potential of the complex scalar field is

$$U(\Phi\Phi^*) = \mu^2\Phi\Phi^*,$$

where Φ is a complex scalar field with conjugate Φ^* and μ is the mass parameter. The complex scalar field are further assumed to take the form:

$$\Phi = \frac{\phi(r)}{\sqrt{2}}e^{-i\omega t}, \quad (2.4)$$

with $\phi(r)$ being a real scalar field and ω the oscillation frequency.

Varying the action (2.1) with respect to $g_{\mu\nu}$, A_μ , and Φ yields the equations of motion:

$$R_{\mu\nu} - \frac{1}{2}g_{\mu\nu}R + g_{\mu\nu}\Lambda - 2\kappa(T_{\mu\nu}^{(1)} + T_{\mu\nu}^{(2)}) = 0, \quad (2.5)$$

$$\nabla_\mu \left(\frac{\partial \mathcal{L}^{(1)}}{\partial \mathcal{F}} F^{\mu\nu} \right) = 0, \quad (2.6)$$

$$\square\Phi - \dot{U}(\Phi\Phi^*)\Phi = 0. \quad (2.7)$$

Here, $\dot{U}(\Phi\Phi^*) = \mu^2$ and the energy-momentum tensors are:

$$T_{\mu\nu}^{(1)} = -\frac{\partial \mathcal{L}^{(1)}}{\partial \mathcal{F}} F_{\mu\rho} F_\nu{}^\rho + g_{\mu\nu} \mathcal{L}^{(1)}, \quad (2.8)$$

$$T_{\mu\nu}^{(2)} = \partial_\mu \Phi^* \partial_\nu \Phi + \partial_\nu \Phi^* \partial_\mu \Phi - g_{\mu\nu} \left[\frac{1}{2} g^{\lambda\rho} (\partial_\lambda \Phi^* \partial_\rho \Phi + \partial_\rho \Phi^* \partial_\lambda \Phi) + U(\Phi, \Phi^*) \right]. \quad (2.9)$$

We consider a static, spherically symmetric spacetime with the metric:

$$ds^2 = -N(r)\sigma^2(r)dt^2 + \frac{dr^2}{N(r)} + r^2(d\theta^2 + \sin^2\theta d\varphi^2), \quad (2.10)$$

where

$$N(r) = 1 - \frac{2Gm(r)}{r} - \frac{\Lambda}{3}r^2.$$

Substituting (2.10) and (2.4) into (2.5) yields the following ordinary differential equations:

$$\phi'' + \left(\frac{2}{r} + \frac{N'}{N} + \frac{\sigma'}{\sigma} \right) \phi' + \left(\frac{\omega^2}{N\sigma^2} - \frac{\mu^2}{2} \right) \frac{\phi}{N} = 0, \quad (2.11)$$

$$N' + \frac{\kappa\omega^2 r \phi^2}{N\sigma^2} + \kappa r N \phi'^2 + \frac{N-1}{r} + \frac{3\kappa\hat{q}^6 r}{s(\hat{q}^3 + r^3)^2} + (\kappa\mu^2\phi^2 + \Lambda)r = 0, \quad (2.12)$$

$$\frac{\sigma'}{\sigma} - \kappa r \left(\phi'^2 + \frac{\omega^2\phi^2}{N^2\sigma^2} \right) = 0, \quad (2.13)$$

where

$$N' = -\frac{2Gm'(r)}{r} + \frac{2Gm(r)}{r^2} - \frac{2\Lambda}{3}r,$$

and “ $'$ ” is used to denote differentiation with respect to r .

To ensure regularity and asymptotic AdS, the following boundary conditions are proposed,

$$m(0) = 0, \quad \sigma(\infty) = 1, \quad (2.14)$$

$$\phi(\infty) = 0, \quad \left. \frac{d\phi}{dr} \right|_{r=0} = 0. \quad (2.15)$$

Moreover, the Arnowitt-Deser-Misner (ADM) mass is given by the asymptotic limit of the solution $m(r)$ as $r \rightarrow \infty$, with $m(\infty) \equiv M$.

3 Numerical scheme

To facilitate our numerical analysis, we introduce dimensionless variables through the following scaling transformations:

$$\begin{aligned} r &\rightarrow \frac{\tilde{r}}{\mu}, & \hat{q} &\rightarrow \frac{\tilde{q}}{\mu}, & \omega &\rightarrow \tilde{\omega}\mu, & \Lambda &\rightarrow \tilde{\Lambda}\mu^2, \\ s &\rightarrow \frac{\kappa\tilde{s}}{\mu^2}, & m &\rightarrow \frac{\tilde{m}}{G\mu}, & \phi &\rightarrow \frac{\tilde{\phi}}{\sqrt{\kappa}}, & M &\rightarrow \frac{\tilde{M}}{G\mu}. \end{aligned} \quad (3.1)$$

After applying these transformations, the form of field equations (2.11)–(2.13) can be simplified by setting:

$$\mu \rightarrow 1, \quad G \rightarrow 1, \quad \text{and} \quad \kappa \rightarrow 1. \quad (3.2)$$

In addition, for the convenience of numerical calculations, a compactified radial coordinate is introduced:

$$x = \frac{\tilde{r}}{1 + \tilde{r}}, \quad (3.3)$$

which maps the physical domain $r \in [0, \infty)$ to the computational domain $x \in [0, 1]$. This transformation yields the following correspondence: $x = 0$ represents the origin (central point of the solution), while $x = 1$ corresponds to spatial infinity.

Finally, the boundary value problem defined by equations (2.11)–(2.13) and the boundary conditions (2.14) and (2.15) is solved using the open-source finite element computing software FEniCSx (version 0.8) [63–66]. We set the computational domain to be discretized with $\geq 10^4$ mesh nodes, and the relative numerical error tolerance is set to $< 10^{-8}$. The smallest frequency parameter considered in our computations is $\tilde{\omega} = 0.0001$. Although solutions for $\tilde{\omega} < 0.0001$ could theoretically be obtained by further refining the mesh, numerical convergence becomes increasingly challenging as the stiffness of the system increases.

4 Numerical results

When $\tilde{\Lambda} = 0$, numerical solutions to equations (2.11)–(2.13) were presented in the literature [62]. A notable feature of these solutions is that they include a *frozen state* configuration with a critical event horizon in the limit $\tilde{\omega} \rightarrow 0$ (practically down to $\tilde{\omega} = 0.0001$). Such solutions endow boson stars with an almost black-hole-like hard boundary, bringing their physical properties closer to those of black holes.

Based on the work presented in [62], we aim to further investigate the existence of such frozen states in the case where $\tilde{\Lambda} \neq 0$. Since the existence of frozen state solutions depends on the value of \tilde{q} , we begin by determining the minimum value of \tilde{q} for which such solutions can exist. This threshold is referred as the *critical value* of q , and denoted by \tilde{q}_c .

The values of \tilde{q}_c corresponding to five typical cosmological constants (0.0, -0.5, -1.0, -1.5, -2.0) are summarized in Table 1. As shown in Table 1, different $\tilde{\Lambda}$ values yield different \tilde{q}_c values, and \tilde{q}_c increases as $\tilde{\Lambda}$ decreases.

Taking the case of $\tilde{\Lambda} = 0$ (where $\tilde{q}_c = 0.49$) as a reference, we classify the magnetic monopole charge parameter \tilde{q} as follows: when $\tilde{q} > 0.49$, it is considered as a *large* one, and when $\tilde{q} < 0.49$, it is considered as a *small* one.

Table 1. Relationship between the cosmological constant $\tilde{\Lambda}$ and the critical magnetic monopole charge \tilde{q}_c . All values are rounded to two decimal places.

$\tilde{\Lambda}$	0.0	-0.5	-1.0	-1.5	-2.0
\tilde{q}_c	0.49	0.51	0.53	0.56	0.58

4.1 ADM Mass

Firstly, for small \tilde{q} , the curve of ADM mass \tilde{M} versus frequency $\tilde{\omega}$ is shown in Fig. 1, with four representative \tilde{q} values (0.0, 0.2, 0.4, 0.45), and $\tilde{s} = 0.2$. The cosmological constant $\tilde{\Lambda}$ is selected from the following discrete set:

$$\tilde{\Lambda} \in \{0.0, -0.02, -0.04, -0.06, -0.08, -0.1\}. \quad (4.1)$$

Our results indicate that the \tilde{M} - $\tilde{\omega}$ curves retain the characteristic spiral structure commonly observed in boson star configurations. Notably, as \tilde{q} increases, the curves become more densely clustered in the low $\tilde{\omega}$ regime, and the range of \tilde{M} variation simultaneously narrows.

To quantitatively assess the influence of $\tilde{\Lambda}$ on \tilde{M} , we selected two key quantities: the maximum ADM mass \tilde{M}_{\max} and the minimum frequency $\tilde{\omega}_{\min}$, and analyzed their variation with $\tilde{\Lambda}$. As shown in Fig. 2, it is found that as $\tilde{\Lambda}$ decreases, \tilde{M}_{\max} monotonically decreases, while $\tilde{\omega}_{\min}$ monotonically increases.

Secondly, for large \tilde{q} , the cosmological constant $\tilde{\Lambda}$ is chosen from the following discrete set:

$$\tilde{\Lambda} \in \{0.0, -0.5, -1.0, -1.5, -2.0, -2.5, -3.0\}. \quad (4.2)$$

The increased interval between $\tilde{\Lambda}$ values (compared to Eq. (4.1)) is selected to avoid overcrowding of the \tilde{M} - $\tilde{\omega}$ curves. Figure 3 shows the \tilde{M} - $\tilde{\omega}$ curve for four typical values of \tilde{q} . As can be seen from Figure 3, as $\tilde{\Lambda}$ increases, the spiral structure disappears, and compared to the case with small \tilde{q} , the overall variation range of \tilde{M} is narrower.

It should be noted that for the $\tilde{M} - \tilde{\omega}$ curve without a spiral structure, the value of $\tilde{\omega}$ can continuously decrease (practically down to $\tilde{\omega} = 0.0001$). This phenomenon will have a significant impact on the structure of spacetime, which will be discussed in 4.2.

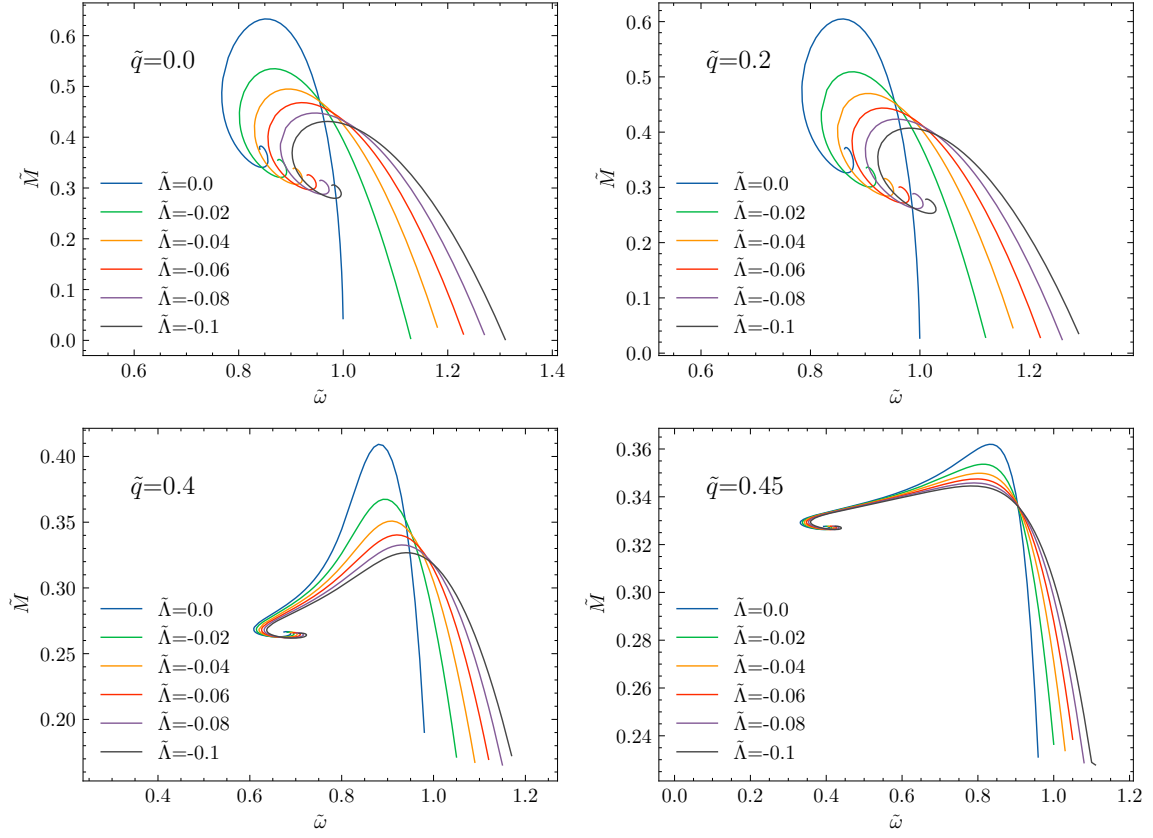


Figure 1. \tilde{M} versus $\tilde{\omega}$ for small \tilde{q} values with $\tilde{s} = 0.2$.

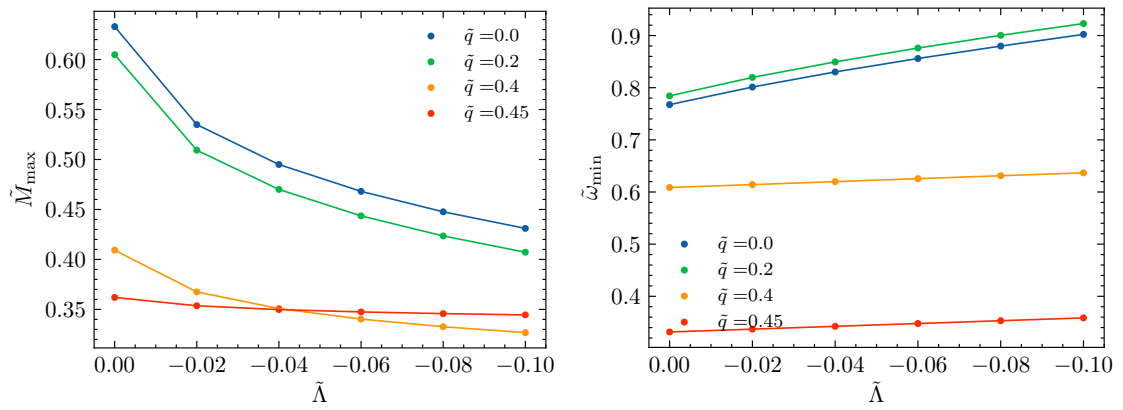


Figure 2. \tilde{M}_{\max} and $\tilde{\omega}_{\min}$ versus $\tilde{\Lambda}$ for small \tilde{q} with $\tilde{s} = 0.2$.

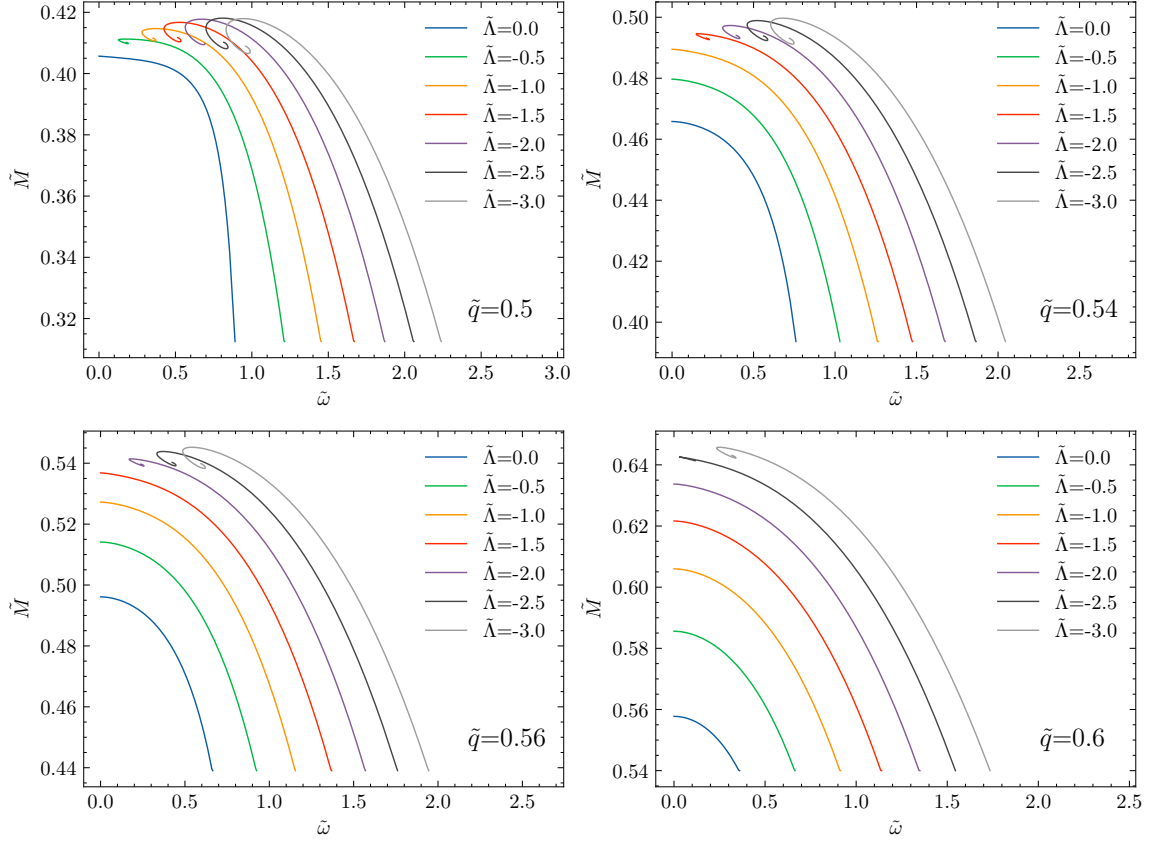


Figure 3. \tilde{M} versus $\tilde{\omega}$ for large \tilde{q} values with $\tilde{s} = 0.2$. The minimum of $\tilde{\omega}$ is 0.0001.

The corresponding dependency of \tilde{M}_{\max} and $\tilde{\omega}_{\min}$ on $\tilde{\Lambda}$ for large \tilde{q} is shown in Fig. 4. Interestingly, \tilde{M}_{\max} now increases monotonically as $\tilde{\Lambda}$ decreases. For $\tilde{\omega}_{\min}$, when its value greater than 0.0001, it also shows a consistent monotonic increase with decreasing $\tilde{\Lambda}$.

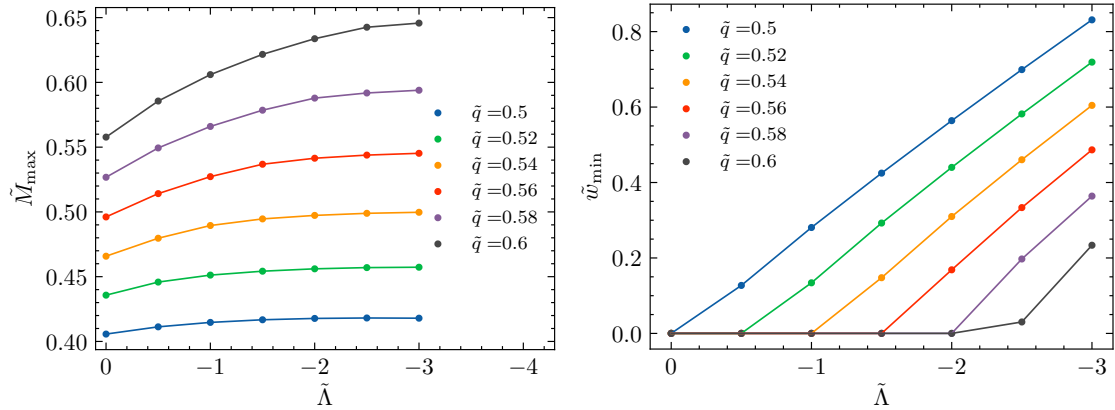


Figure 4. \tilde{M}_{\max} and $\tilde{\omega}_{\min}$ versus $\tilde{\Lambda}$ for large \tilde{q} with $\tilde{s} = 0.2$.

4.2 Frozen States and Critical Horizon

First, the effect of the continuously decreasing $\tilde{\omega}$ on the solutions to the equations of motion is discussed. A set of numerical results for typical \tilde{q} and $\tilde{\Lambda}$ values is displayed in Figure 5, revealing that a significant increase in the absolute values of the $\tilde{\phi}$ and σ gradients near $x = 0.34$ is induced by reducing $\tilde{\omega}$. This behavior is demonstrated below to have a substantial impact on metrics.

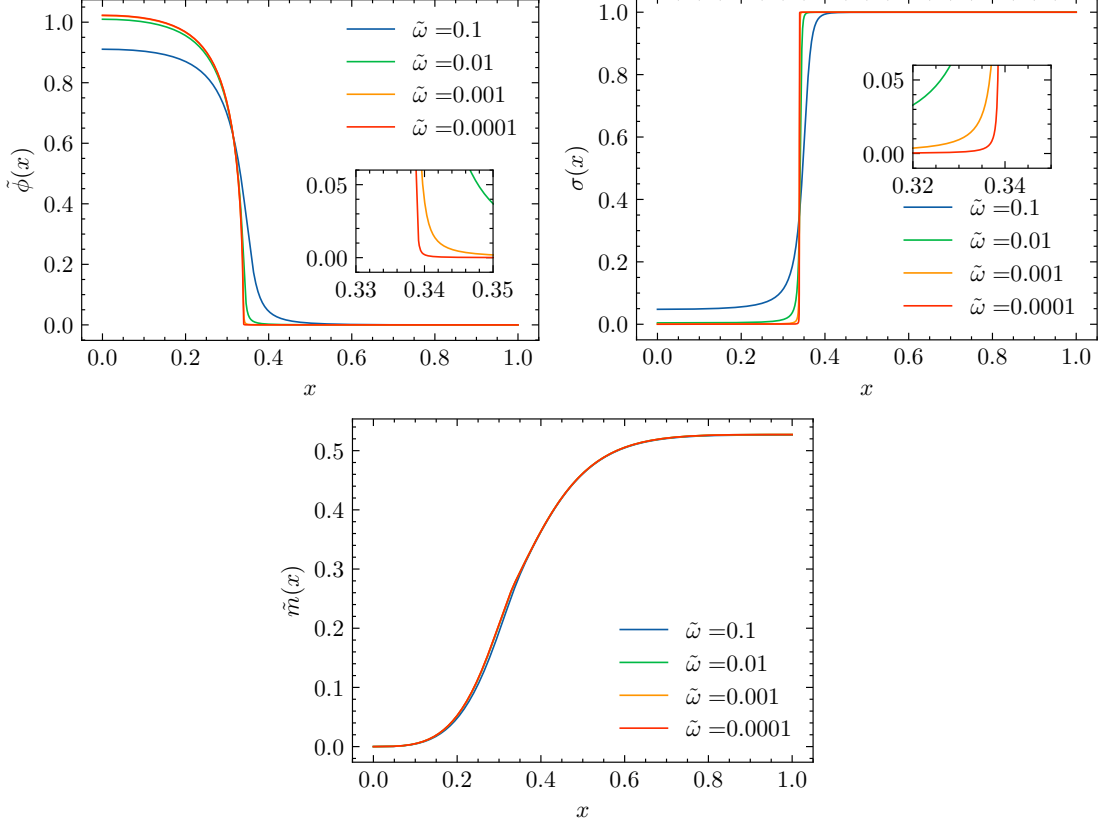


Figure 5. Solutions for $\tilde{q} = 0.56$, $\tilde{\Lambda} = -1.0$, and $\tilde{s} = 0.2$ under varying $\tilde{\omega}$ values.

Figure 6(a) and Figure 6(b) show the variation of $-g_{tt}$ and g^{rr} with $\tilde{\omega}$. It can be observed that as $\tilde{\omega}$ decreases, the minimum values of $-g_{tt}$ and g^{rr} continue to decrease. When $\tilde{\omega}$ approaches 0.0001, there exists a region centered at $x = 0$ where $-g_{tt}$ significantly decreases to the order of $\mathcal{O}(10^{-7})$. Meanwhile, the minimum value of g^{rr} also drops to the same order. If defining the boundary of this region as x_c , as shown in Figure 6(b), the value of x_c can be precisely determined using the minimum value of g^{rr} .

A further analysis of the metric components is presented in Figs. 6(c) and 6(d), which display the solutions for different $\tilde{\Lambda}$ and \tilde{q} values at a fixed $\tilde{\omega} = 0.0001$. The curves demonstrate identical profiles for both $-g_{tt}$ and g^{rr} in the region $x > x_c$, while in the interior region ($x < x_c$), the value of $-g_{tt}$ maintains at the order of $\mathcal{O}(10^{-7})$.

As $x \rightarrow x_c$, $-g_{tt} \rightarrow 0$. For a distant observer, time near x_c slows down infinitely, causing matter to asymptotically approach—but never cross—the surface at x_c within finite

time. This behavior aligns with the definition of a "frozen star" [67]. However, due to the limitations of numerical computation, we cannot obtain a solution where $-g_{tt}|_{x \rightarrow x_c} \rightarrow 0$ in practice. Therefore, we conclude that when $\tilde{\omega} = 0.0001$ and $-g_{tt}|_{x \rightarrow x_c} \approx 10^{-7}$, the boson star is in a "frozen state" [62, 68, 69], and call x_c the *critical horizon* radius. The critical horizon radius \tilde{r}_c^H in the physical coordinate system is then given by:

$$\tilde{r}_c^H = \frac{x_c}{1 - x_c}.$$

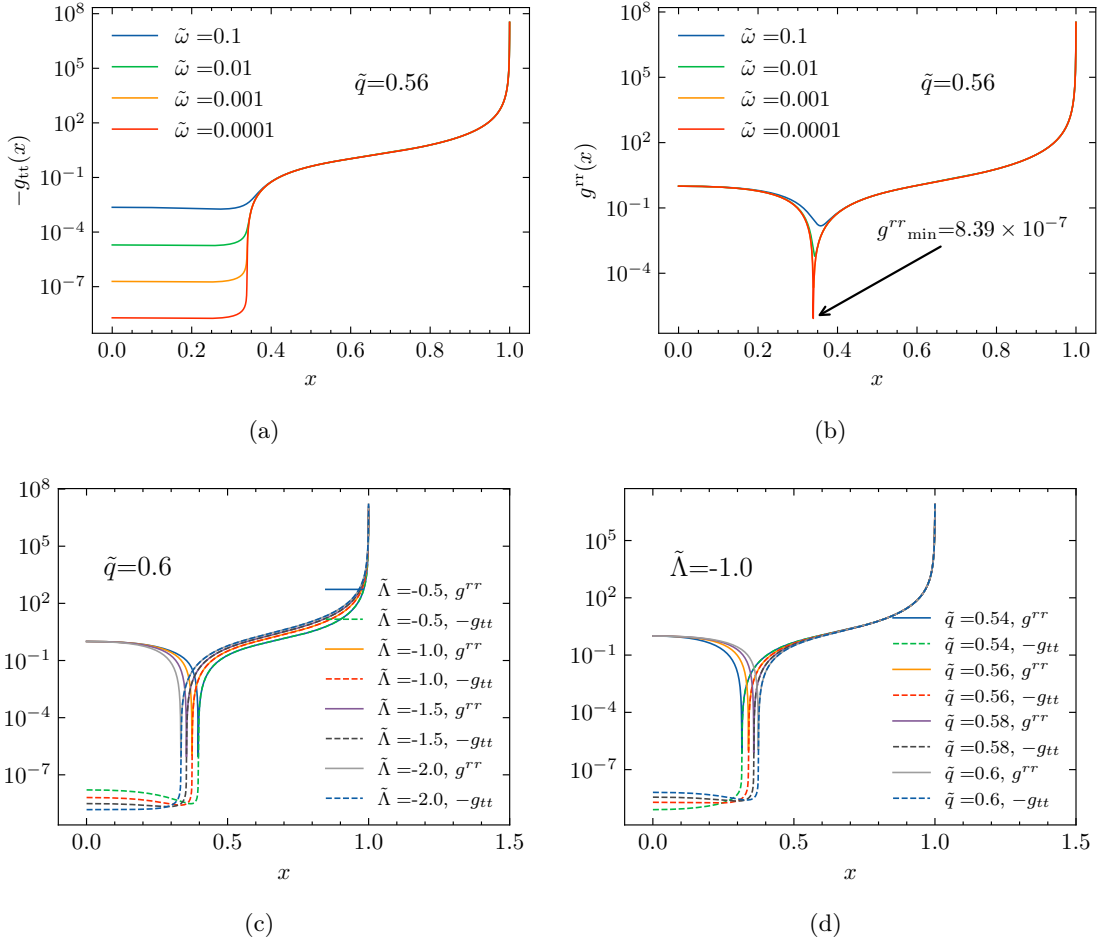


Figure 6. Plots of metric components $-g_{tt}$ and g^{rr} .

Further, Figure 7 illustrates how $\tilde{\Lambda}$ affects both the ADM mass and critical horizon radius \tilde{r}_c^H of boson star at frozen state. The ADM mass shows a monotonic increase with decreasing $\tilde{\Lambda}$, while \tilde{r}_c^H follows an opposite trend, decreasing monotonically as $\tilde{\Lambda}$ decreases. If defining \tilde{r}_c^H as the effective radius of a boson star, that implies the compactness of the boson star increases as $\tilde{\Lambda}$ decreases.

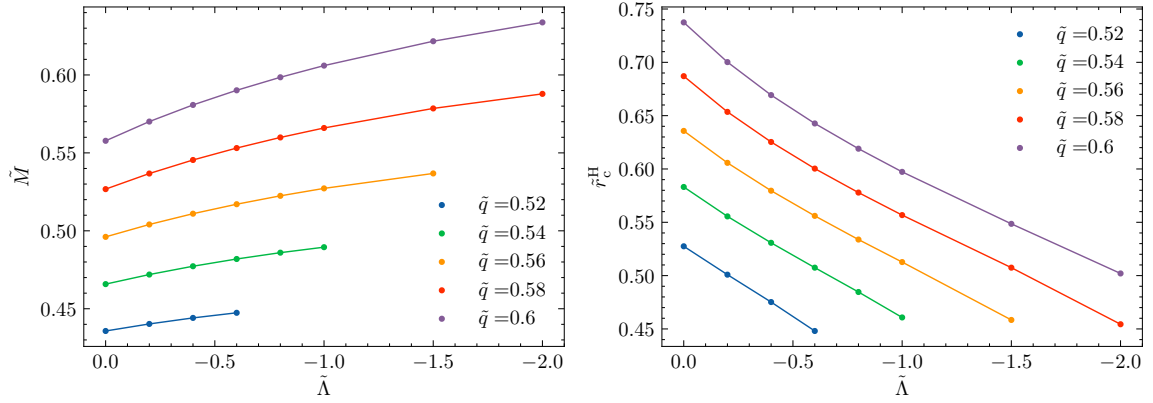


Figure 7. ADM mass and critical horizon radius \tilde{r}_c^H versus $\tilde{\Lambda}$ for frozen states ($\tilde{\omega} = 0.0001$) with $\tilde{s} = 0.2$.

4.3 Light Rings

The geodesic equation for particles in a gravitational field is

$$g_{\mu\nu}\dot{x}^\mu\dot{x}^\nu = -\epsilon, \quad (4.3)$$

where the dot denotes differentiation with respect to the affine parameter (for photons) or proper time (for massive particles) along the geodesic. Here, $x^\mu = (t, \tilde{r}, \theta, \varphi)$ represents the coordinate components, with $\epsilon = 0$ and $\epsilon = 1$ corresponding to photons and massive particles, respectively.

Due to the static spherical symmetry, we assume particles' orbits lie in the equatorial plane $\theta = \pi/2$, implying $\dot{\theta} = 0$. The metric (2.10) possesses two Killing vectors ∂_t and ∂_φ , corresponding to conserved quantities: the energy $E = -g_{tt}\dot{t}$ and angular momentum $L = \tilde{r}^2\dot{\varphi}$. Equation (4.3) then reduces to

$$\frac{1}{2}\dot{\tilde{r}}^2 + V(\tilde{r}) = 0, \quad (4.4)$$

with

$$V(\tilde{r}) = \frac{1}{2} \frac{1}{g_{tt}g_{rr}} \left(E^2 + g_{tt} \left(\epsilon + \frac{L^2}{\tilde{r}^2} \right) \right). \quad (4.5)$$

For photons, the effective potential is defined as:

$$V_{\text{eff}}^{\text{pho}}(\tilde{r}) = -\frac{g_{tt}}{\tilde{r}^2}. \quad (4.6)$$

The conditions for stable circular motion of photons are:

$$V(\tilde{r}) = 0, \quad V_{\text{eff}}^{\text{pho}'}(\tilde{r}) = 0 \quad \text{and} \quad V_{\text{eff}}^{\text{pho}''}(\tilde{r}) > 0.$$

The stability of the orbit along the θ -direction of boson stars has been rigorously proved by Cunha, Berti and Herdeiro [70].

Figure 8 shows the effective potential curves corresponding to two typical parameter combinations (\tilde{q} and $\tilde{\Lambda}$). From the figure, it can be observed that each effective potential curve has two extreme points, which means there are two light rings (LRs) [71]. The positions of the extreme points indicate that the inner light ring is stable while the outer one is unstable.

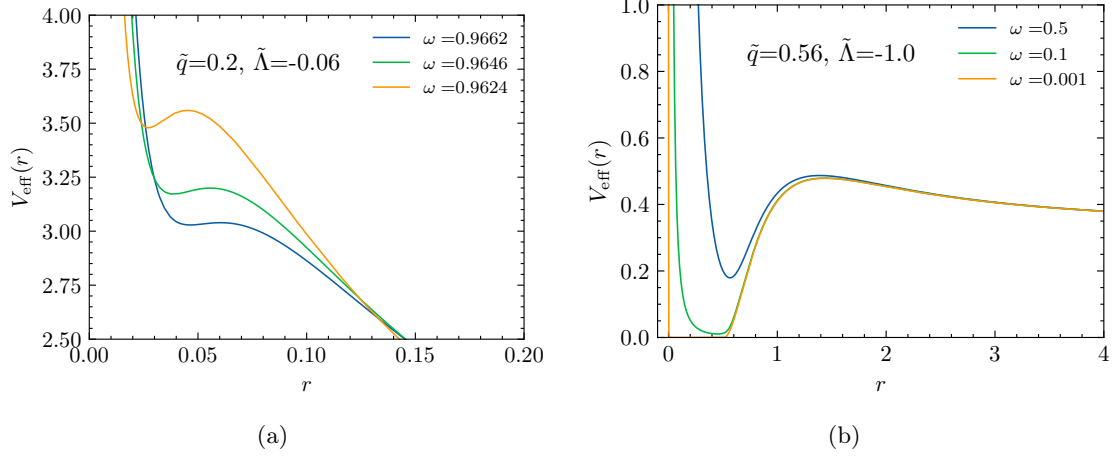


Figure 8. Effective potentials for photon circular orbits with (a) $\tilde{q} = 0.2$, $\tilde{\Lambda} = -0.06$ and (b) $\tilde{q} = 0.56$, $\tilde{\Lambda} = -1.0$.

Our further calculations reveal that LR exists for all combinations of \tilde{q} and $\tilde{\Lambda}$ with

$$\tilde{q} \in \{0.0, 0.2, 0.4, 0.45\}, \quad \tilde{\Lambda} \in \{0.0, -0.02, -0.04, -0.06, -0.08, -0.1\},$$

and

$$\tilde{q} \in \{0.5, 0.52, 0.54, 0.56, 0.58, 0.60\},$$

$$\tilde{\Lambda} \in \{0.0, -0.2, -0.4, -0.5, -0.6, -0.8, -1.0, -1.5, -2.0, -2.5, -3.0\}.$$

The existence domains of LR solutions are illustrated in Figures 9 and 10, where the shaded regions along the \tilde{M} - $\tilde{\omega}$ curves indicate the parameter ranges supporting LR solutions. We find that as \tilde{q} increases, the LR solutions gradually extend their coverage along the \tilde{M} - $\tilde{\omega}$ curves, eventually spanning the entire curve when \tilde{q} becomes sufficiently large.

Further, the $\tilde{\omega}$ dependence of these LR radii is presented in Figure 11 for some large values of \tilde{q} and a broader range of $\tilde{\Lambda}$ values, where the inner and outer radii are denoted by $\tilde{r}_{\text{inner}}^{\text{LR}}$ and $\tilde{r}_{\text{outer}}^{\text{LR}}$, respectively. From the figure, it is found that: (1) as $\tilde{\Lambda}$ is decreased, the relationship between $\tilde{r}_{\text{inner}}^{\text{LR}}$ and $\tilde{r}_{\text{outer}}^{\text{LR}}$ is changed from linear to nonlinear; and (2) as $\tilde{\omega}$ is increased, the radii $\tilde{r}_{\text{inner}}^{\text{LR}}$ and $\tilde{r}_{\text{outer}}^{\text{LR}}$ are brought increasingly close.

To intuitively demonstrate the quantitative relationship between the LR radii and the critical horizon radius of frozen boson stars, as well as their dependence on $\tilde{\Lambda}$, their numerical values are presented in Figure 12. It is shown that both the inner LR radius and critical horizon radius are increased monotonically as $\tilde{\Lambda}$ is decreased, while the outer LR radius is observed to exhibit an opposite trend, being decreased monotonically with $\tilde{\Lambda}$.

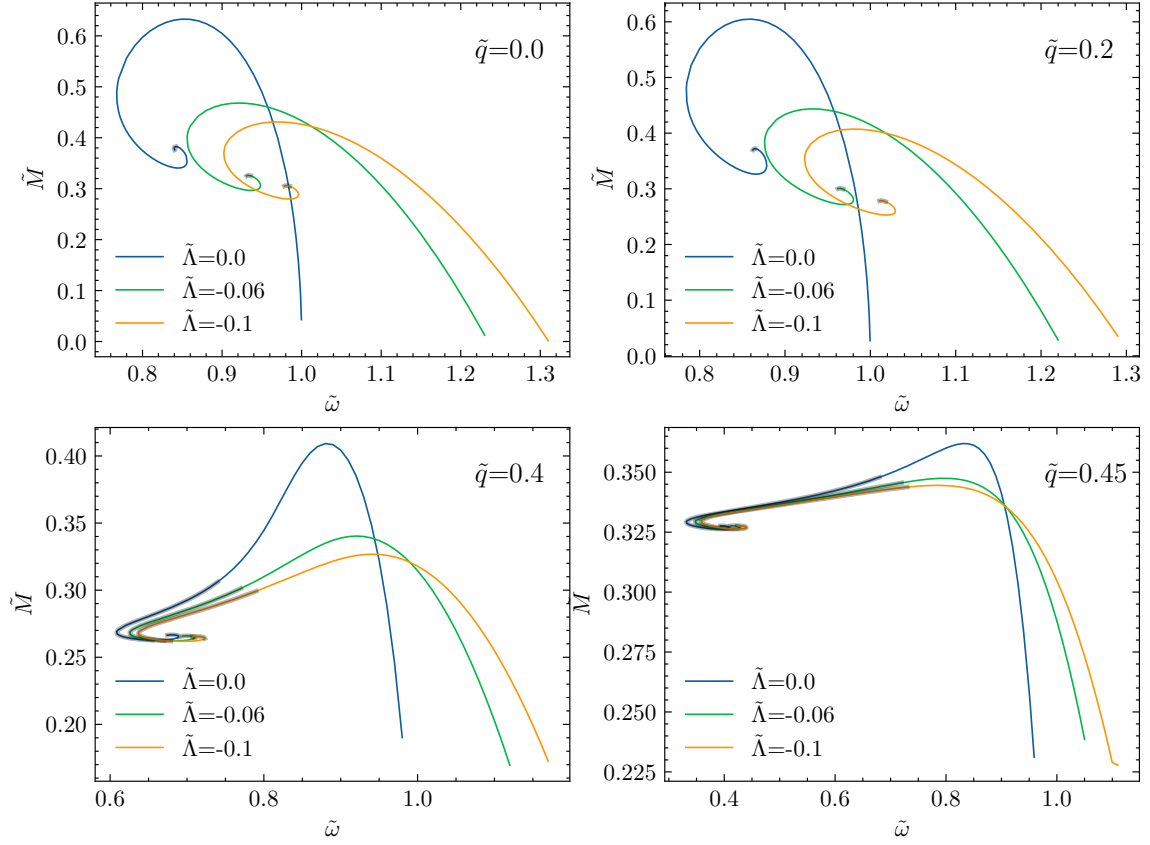


Figure 9. The existence region (shaded) of LR solutions on the \tilde{M} - $\tilde{\omega}$ curve for small \tilde{q} with $\tilde{s} = 0.2$.

Furthermore, the inner light ring is always located within the critical horizon ($\tilde{r}_{\text{inner}}^{\text{LR}} < x_c$), while the outer light ring is consistently positioned outside this boundary ($\tilde{r}_{\text{outer}}^{\text{LR}} > x_c$).

To determine photon trajectories orbiting a photon sphere, we numerically solve Equation (4.4). Introducing the substitution $u = 1/\tilde{r}$ [72] and using angular momentum conservation ($L = \tilde{r}^2 \dot{\varphi}$), Equation (4.4) may be transformed to:

$$\left(\frac{du}{d\varphi}\right)^2 + \frac{1}{g_{tt}g_{rr}} \left(g_{tt}u^2 + \frac{1}{b^2}\right) = 0, \quad (4.7)$$

where $b = L/E$ is the impact parameter. Differentiating (4.7) with respect to φ yields

$$\frac{d^2u}{d\varphi^2} + \frac{1}{2b^2u^2g_{rr}g_{tt}} \left(\frac{1}{g_{rr}} \frac{dg_{rr}}{d\tilde{r}} + \frac{1}{g_{tt}} \frac{dg_{tt}}{d\tilde{r}}\right) + \frac{u}{g_{rr}} + \frac{1}{2g_{rr}^2} \frac{dg_{rr}}{d\tilde{r}} = 0. \quad (4.8)$$

Substituting metric (2.10) gives the simplified form

$$\frac{d^2u}{d\varphi^2} = \frac{\sigma'}{b^2u^2\sigma^3} + \frac{N'}{2} - uN. \quad (4.9)$$

Numerical integration of this equation determines the photon trajectory.

Figure 13 illustrates a typical halo image obtained through numerical integration. The gray disk in the figure corresponds to the region within the critical horizon radius, while

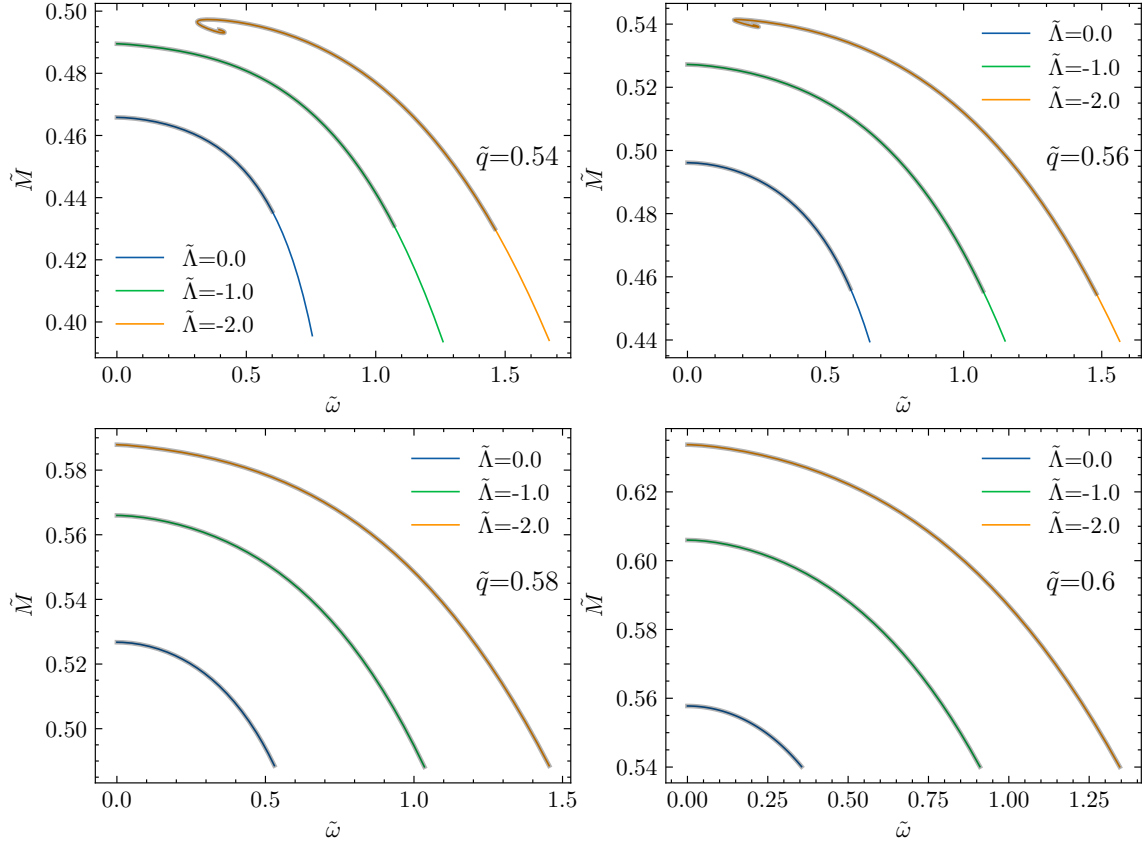


Figure 10. The existence region (shaded) of LR solutions on the $\tilde{M} - \tilde{\omega}$ curve for large \tilde{q} with $\tilde{s} = 0.2$.

the blue ring depicts the trajectory of photons completing two full orbits. The red marker indicates the emission point, where photons are emitted vertically upward.

The images reveal that as the parameter $\tilde{\Lambda}$ decreases, both the critical horizon radius and the inner light ring shrink, whereas the outer light ring exhibits a clear expansion. These phenomena are consistent with the results presented in Figure 12.

4.4 Accretion Disk and Shadows

Here we assume that (1) the accretion disk is geometrically thin and optically thick [73, 74], and (2) the observer's reference frame is at rest relative to the boson star, satisfying the zero angular momentum observer (ZAMO) condition.

For massive particles, the effective potential is given by

$$V_{\text{eff}}^{\text{par}}(\tilde{r}) = -g_{tt} \left(1 + \frac{L^2}{\tilde{r}^2} \right). \quad (4.10)$$

The conditions for stable circular motion require

$$V(\tilde{r}) = 0, \quad V_{\text{eff}}^{\text{par}'}(\tilde{r}) = 0 \quad \text{and} \quad V_{\text{eff}}^{\text{par}''}(\tilde{r}) > 0, \quad (4.11)$$

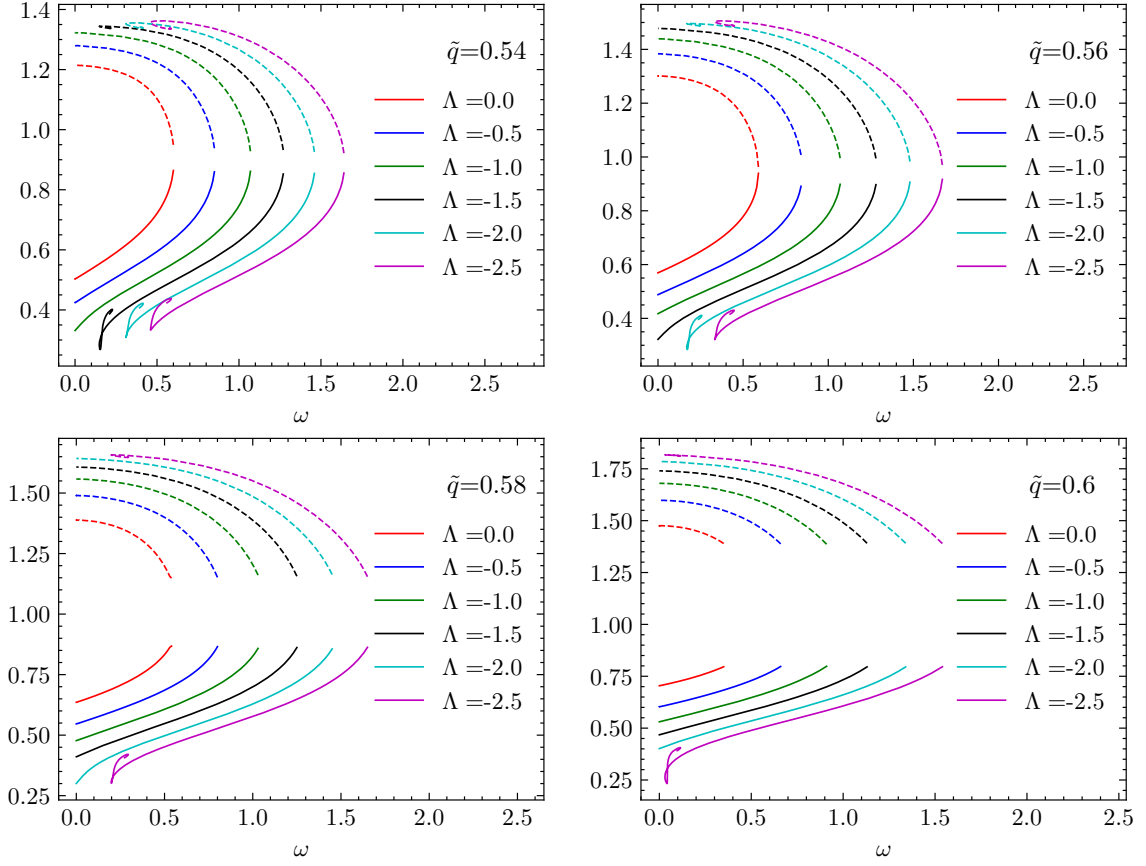


Figure 11. $\tilde{r}_{\text{inner}}^{\text{LR}}$ (solid lines) and $\tilde{r}_{\text{outer}}^{\text{LR}}$ (dashed lines) versus $\tilde{\omega}$ with $\tilde{s} = 0.2$.

where the innermost stable circular orbit (ISCO) satisfies $V_{\text{eff}}^{\text{par}''}(\tilde{r}_{\text{ISCO}}) \rightarrow 0$. The angular velocity Ω , angular momentum L , and energy E of a massive particle performing circular motion are:

$$\Omega = \frac{d\varphi}{dt} = \sqrt{\frac{-\partial_r g_{tt}}{\partial_r g_{\varphi\varphi}}}, \quad (4.12)$$

$$L = \frac{g_{\varphi\varphi}\Omega}{\sqrt{-g_{tt} - g_{\varphi\varphi}\Omega^2}}, \quad (4.13)$$

$$E = -\frac{g_{tt}}{\sqrt{-g_{tt} - g_{\varphi\varphi}\Omega^2}}. \quad (4.14)$$

Fig. 14 shows the variations of \tilde{r}_{ISCO} , L_{ISCO} , and E_{ISCO} with respect to $\tilde{\Lambda}$. We find that \tilde{r}_{ISCO} reaches its maximum value at $\tilde{\Lambda} = 0$, with only minor variations thereafter. Meanwhile, both L_{ISCO} and E_{ISCO} exhibit monotonic decreases with increasing $\tilde{\Lambda}$.

Fig. 15 presents the dependence of \tilde{r}_{ISCO} , L_{ISCO} , and E_{ISCO} on $\tilde{\omega}$, and $\tilde{\omega} \in \{0.0001, 0.001, 0.01, 0.1, 0.2, 0.3, 0.4, 0.5\}$. Our results indicate that all three parameters show slight increases as $\tilde{\omega}$ decreases.

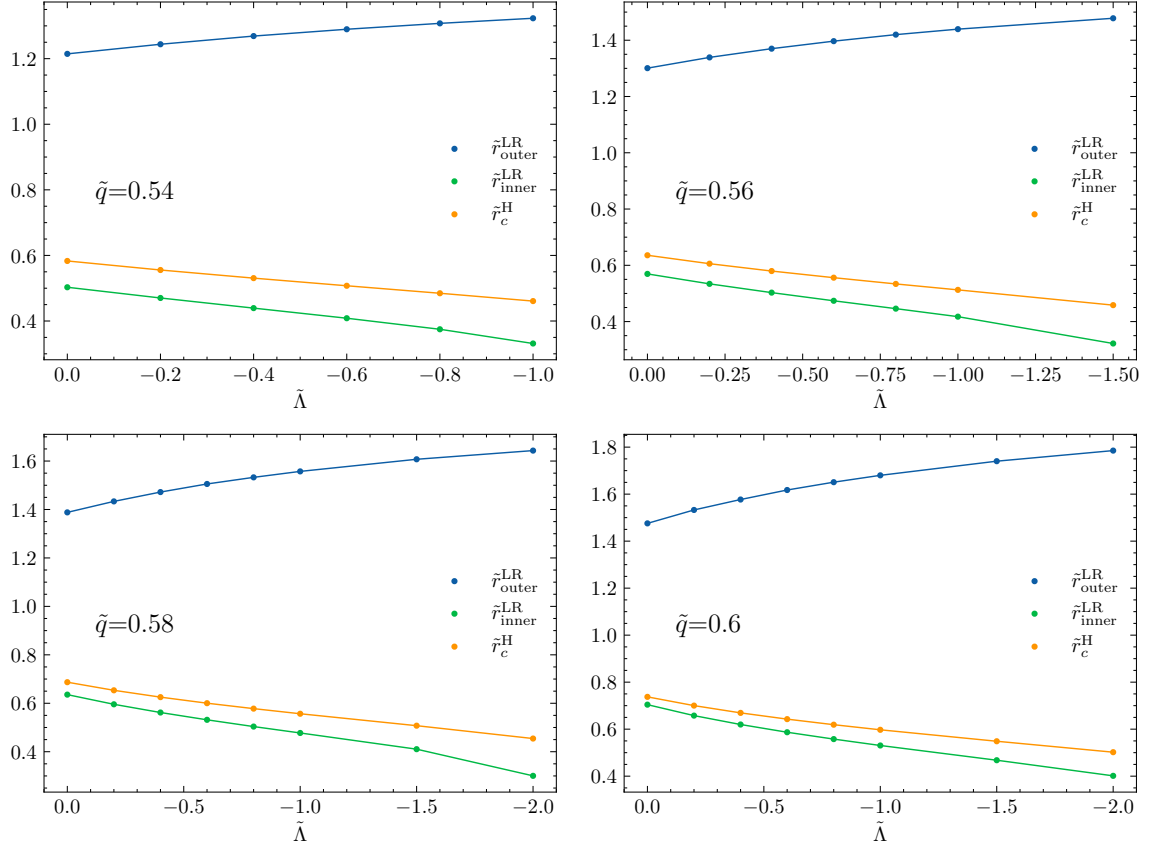


Figure 12. \tilde{r}_c^H , $\tilde{r}_{\text{inner}}^{\text{LR}}$ and $\tilde{r}_{\text{outer}}^{\text{LR}}$ versus $\tilde{\Lambda}$ for $\tilde{\omega} = 0.0001$ and different values of \tilde{q} with $\tilde{s} = 0.2$.

In order to obtain images of the accretion disk using ray tracing methods, we adopt the following coordinate system configuration: (1) The boson star's center coincides with the coordinate origin. (2) The accretion disk lies in the X-Y plane. (3) The position vector \vec{r} of the screen's center o resides in the X-Z plane, forming an angle θ with the Z-axis, with \vec{r} being normal to the screen plane. (4) For any pixel on the screen, its position vector relative to o makes an angle α with the y -axis (as shown in Fig. 16).

Let E_{em} denote the energy of photons emitted from the accretion disk, and E_{obs} denote the energy received by the observer. Incorporating both gravitational redshift and Doppler effects, the redshift factor can be expressed as [72]

$$1 + z = \frac{E_{\text{em}}}{E_{\text{obs}}} = \frac{1 + \Omega b \sin \theta_0 \cos \alpha}{\sqrt{-g_{tt} - g_{\phi\phi} \Omega^2}} \bigg|_{\tilde{r}=\tilde{r}_d}, \quad (4.15)$$

where \tilde{r}_d denotes the radial coordinate of the particles on disk.

Using the fixed observation frequencies of the Event Horizon Telescope (EHT) (1.3 mm [75] or 0.87 mm [76]), we can invert the emission spectrum distribution of the accretion disk through Equation (4.15). Defining λ_0 as the observed wavelength and λ as the emission

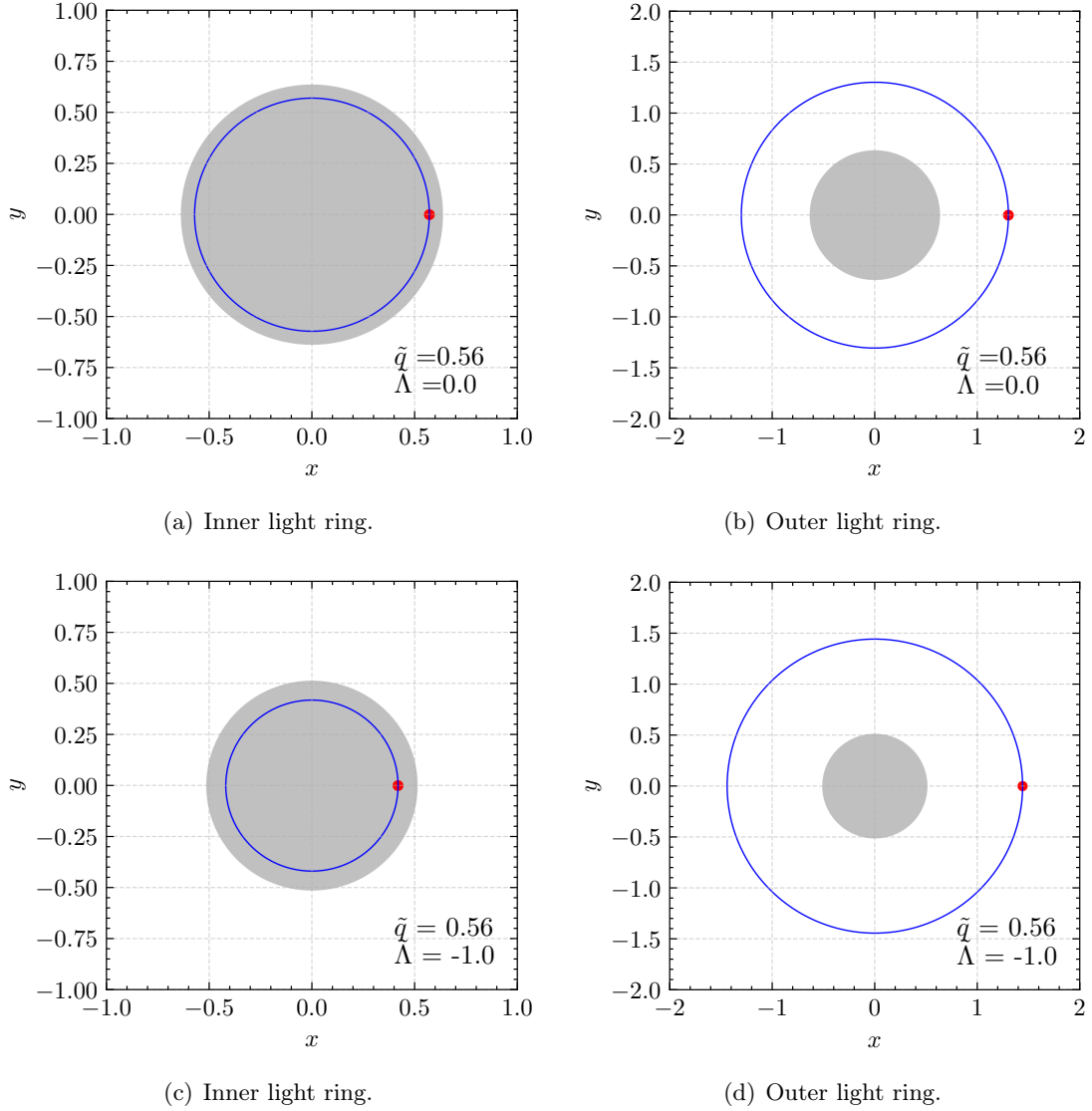


Figure 13. Light rings with the parameter $\tilde{\omega} = 0.0001$. The gray disk in the image corresponds to the region within the critical horizon radius, while the red marker indicates the emission point position (assuming vertical upward photon emission). The blue circle represents the photon trajectory after completing two full orbits.

wavelength from the disk, they satisfy:

$$\lambda = \frac{\lambda_0}{1+z}. \quad (4.16)$$

By mapping the calculation results to the 420-660 nm visible light range, we can obtain the pseudo-color image of the accretion disk radiation spectral distribution.

Fig. 17 displays the detectable spectral distribution of the accretion disk under the conditions $\lambda_0 = 0.87$ mm, $\tilde{\Lambda} = 0.0$, and $\tilde{q} = 0.56$. Given that $\tilde{r}_{\text{ISCO}} = 2.75$, we set the inner disk radius to 2.75 and the outer radius to 10. The distance between the boson star

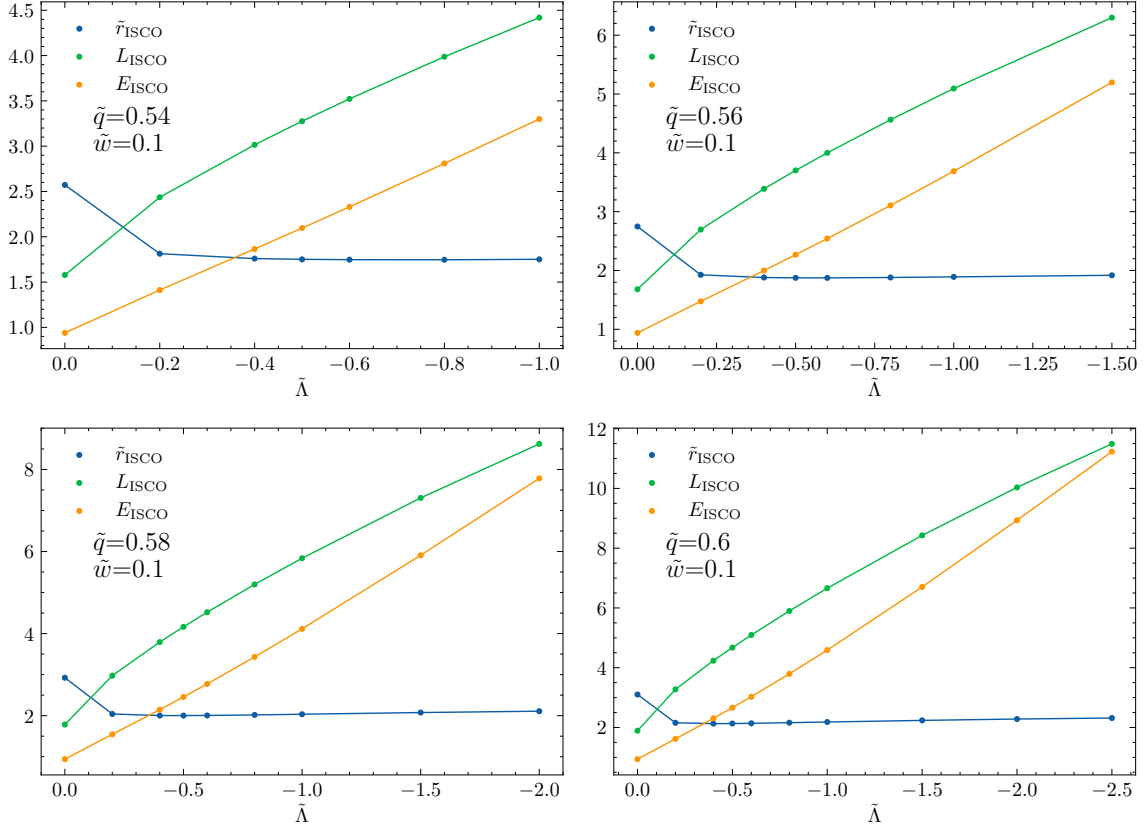


Figure 14. \tilde{r}_{ISCO} , L_{ISCO} , and E_{ISCO} versus $\tilde{\Lambda}$ for $\tilde{q} = 0.56$

and the observer is set to $\tilde{r}_{\text{obs}} = 100$, and the field of view (fov) of the observer is 15° . It should be noted that in order to clearly display the secondary images (*photon ring*) inside the *shadow* region at the center, we adjusted the background color to *white*.

The first row in Fig. 17 shows imaging results at different inclination angles for $\tilde{\omega} = 0.1$. Fig. 17a from outside to inside is divided into three discontinuous regions, they are correspond to primary image, secondary image I, and the secondary image II, respectively. Where the primary image and secondary image II correspond to the upper side of the disk, while the secondary image I correspond to the lower side of the disk, respectively. This phenomenon of multiple secondary images appearing in the shadow region has also been observed recently in other studies [46, 77–81]. Based on this characteristic, the observed target can be ruled out as a Schwarzschild black hole.

To elucidate the image configuration of the Fig. 17a, Fig. 18 illustrates the correspondence between photon trajectories and spectral images. In Fig. 18a: Ray 1 corresponds to the primary image, in which the position vector of photons (relative to the boson star center) rotates $\pi/2$ from the observer to the disk; Ray 2 correspond to the secondary image I, in which the position vector of photons rotates $3\pi/2$; Ray 3 correspond to the secondary image II, in which the position vector of photons rotates $5\pi/2$ and its trajectory exhibits

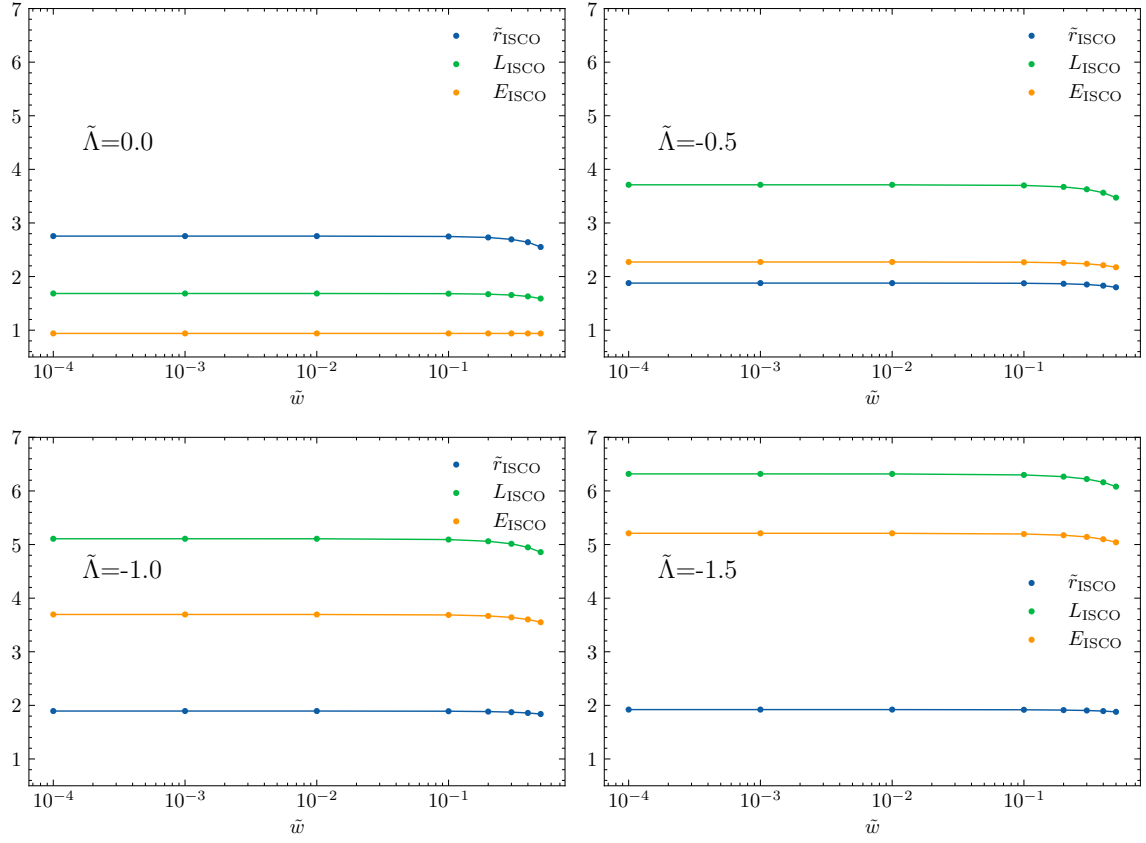


Figure 15. \tilde{r}_{ISCO} , L_{ISCO} , and E_{ISCO} versus $\tilde{\omega}$ for $\tilde{q} = 0.56$. The minimum of $\tilde{\omega}$ is 0.0001.

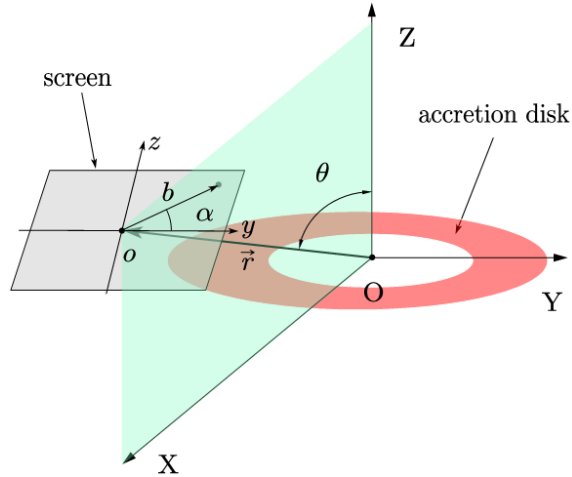


Figure 16. Schematic diagram of the coordinate system configuration. The X-Z plane is shaded in light green. The screen center's position vector \vec{r} lies in the X-Z plane and \vec{r} is normal to the screen surface. The accretion disk lies within the equatorial X-Y plane. When viewed from the negative Z-axis direction, the accretion disk rotates counterclockwise.

double inflection points.

The spectral distribution of secondary image II is different from that of secondary image I. In order to see that clearly, we present an enlarged view of the Fig. 18b in Fig. 19. From Fig. 19a, we observe that the wavelength increases gradually from the inside to the outside on the secondary image, a distribution consistent with that of the primary image. In contrast, as shown in Fig. 19b, the wavelength on the secondary image II decreases from the inside to the outside.

To better understand the spectral distribution in Fig. 19b, we show in Fig. 20 the relationship between the intersection points of photon trajectories with the accretion disk and the corresponding incident angles. Here, the incident angle refers to the angle between the light from the observer and the line connecting the observer and the center of the boson star. It can be seen that as the incident angle decreases, the intersection points move progressively from the inner to the outer regions of the disk. This results in a corresponding decrease in observed wavelength from the inside to the outside in the spectrum.

The second row of Fig. 17 presents results for $\tilde{\omega} = 0.0001$, at this point, the boson star is frozen, the existence of a critical event horizon leads to omission of light rays crossing the horizon, resulting in the absence of secondary image II. So the image of the accretion disk near the boson star resembles that of a Schwarzschild black hole.

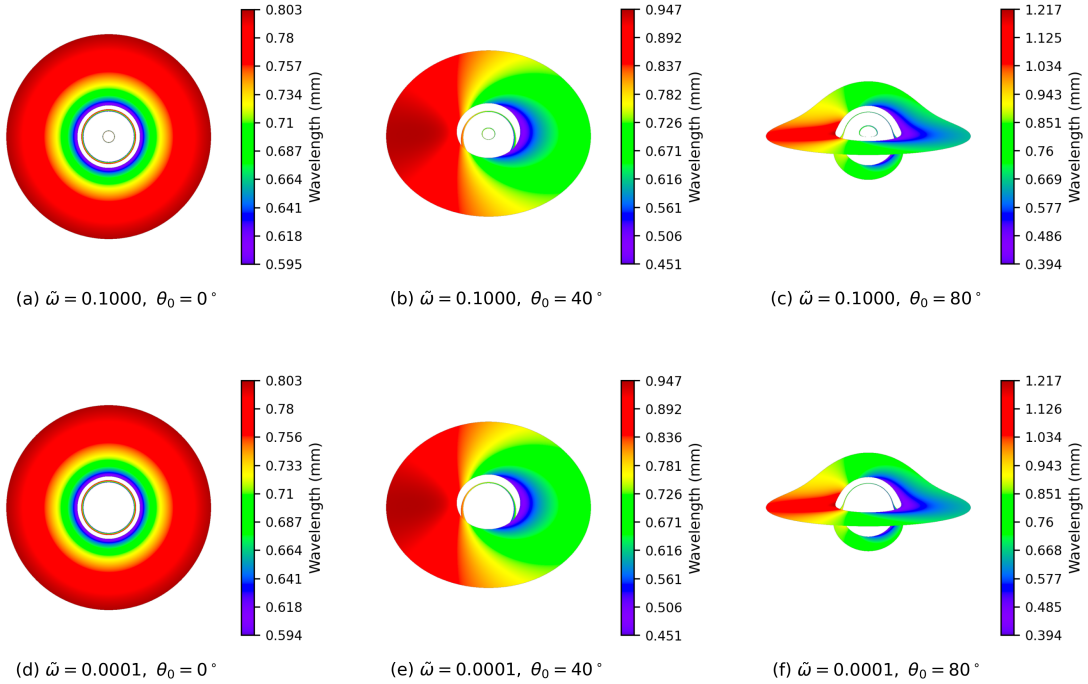


Figure 17. Shadows and spectral distribution on the accretion disk with $\tilde{\Lambda} = 0.0$ and $\tilde{q} = 0.56$. First row $\tilde{\omega} = 0.1$ and second row $\tilde{\omega} = 0.0001$. Columns from left to right correspond to inclination angles of 0° , 40° , and 80° respectively, with disk radii ranging from 2.75 to 10 and $\lambda_0 = 0.87$ mm. To clearly display the secondary image inside the shadow region, we adjusted the background color to *white*.

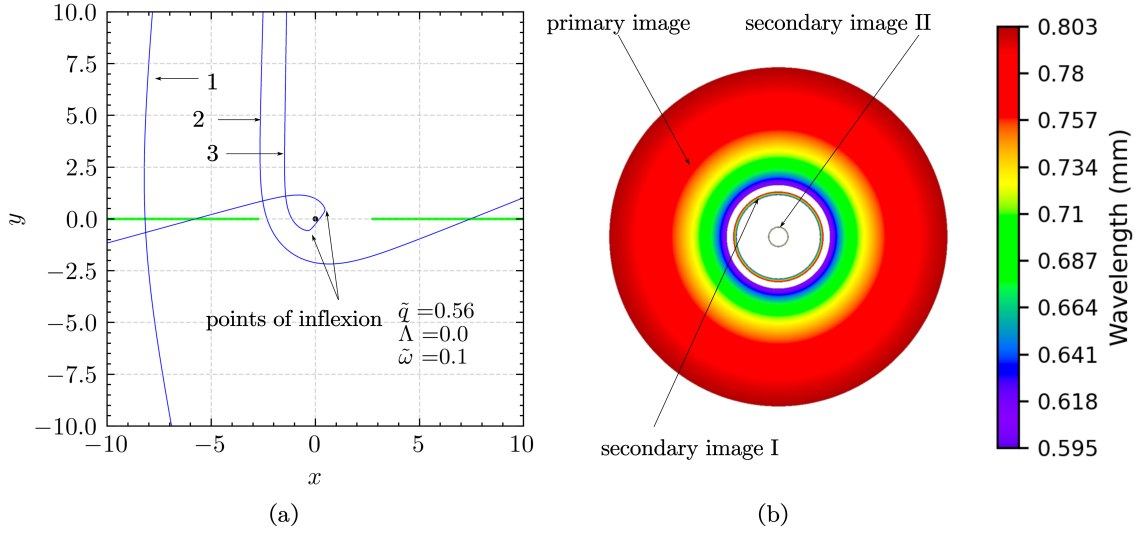


Figure 18. (a) Photon trajectory cross-section ($\tilde{q} = 0.56$, $\tilde{\Lambda} = 0$, $\tilde{w} = 0.1$), where the green horizontal line indicates the accretion disk position, black dot marks the boson star center. The incident angles of light rays 1, 2, and 3 are 5.0° , 1.6° and 0.88° , respectively. Light rays 1, 2, and 3 are the representative ones associated with primary image, secondary image I, and secondary image II of (b), respectively.

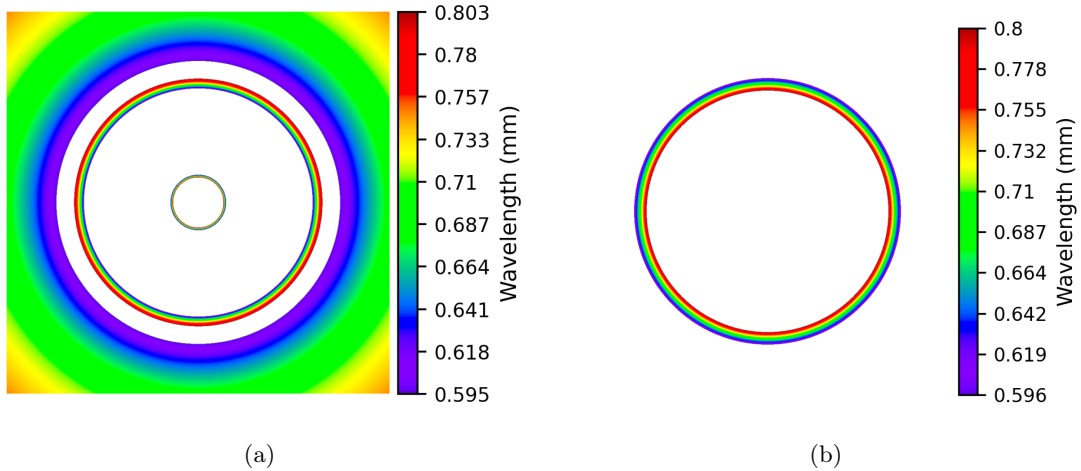


Figure 19. Magnified view of the central region in Figure 18b, with (a) $\text{fov} = 5^\circ$, and (b) $\text{fov} = 1^\circ$ (only secondary image II).

Fig. 21 shows the shadows and spectral distribution for $\tilde{\Lambda} = -1.0$. Compared with Fig. 17, wavelength variations are more pronounced at non-zero inclination angles.

It is noteworthy that for small inclination angles (0° or 40°), the ISCO region covers the secondary image I; whereas for large inclination angles (80°), as shown in Fig. 22, the secondary image remains visible in the shadow region and below the disk.

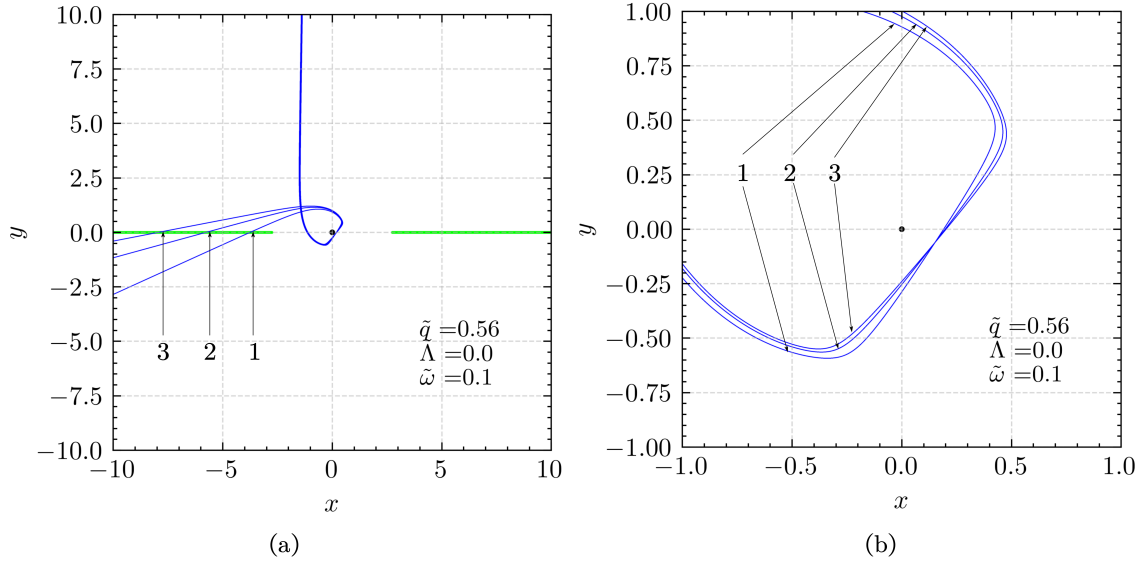


Figure 20. The incident angles of light rays 1, 2, and 3 are 0.9° , 0.88° and 0.87° , respectively.

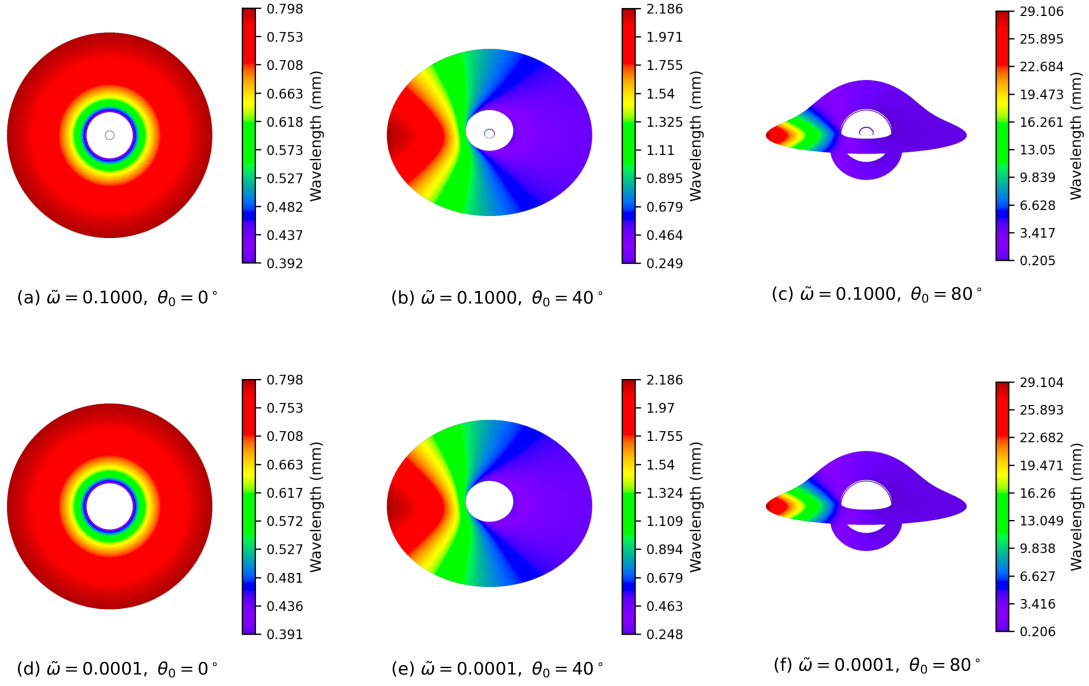


Figure 21. Shadows and spectral distribution on the accretion disk with $\tilde{\Lambda} = -1.0$ and $\tilde{q} = 0.56$. First row $\tilde{\omega} = 0.1$ and second row $\tilde{\omega} = 0.0001$. Inclination angles from left to right are 0° , 40° , and 80° respectively, with disk radii from 1.9 to 10 and $\lambda_0 = 0.87$ mm.

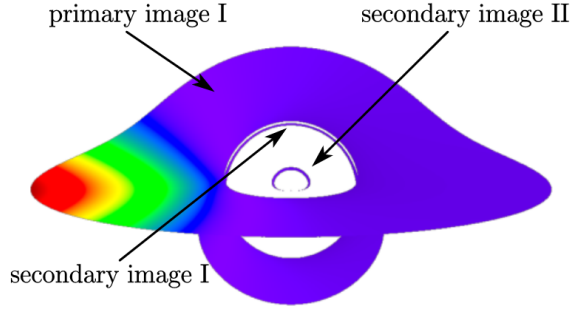


Figure 22. Magnified view of Fig. 21c.

5 Conclusion

In this paper, we investigated some fundamental properties of Hayward mini-boson stars in asymptotically Anti-de Sitter (AdS) spacetime, focusing on their solutions, light ring structures, shadow features, and accretion disk observable spectral distribution. By solving the coupled Einstein-nonlinear electrodynamics-scalar field equations numerically, our main findings are as follows:

Firstly, the maximum ADM mass \tilde{M}_{\max} and the minimum frequency $\tilde{\omega}_{\min}$ exhibit a clear dependence on the cosmological constant $\tilde{\Lambda}$. For small magnetic monopole charge \tilde{q} , \tilde{M}_{\max} decreases monotonically as $\tilde{\Lambda}$ decreases, while $\tilde{\omega}_{\min}$ increases monotonically. In the case of large \tilde{q} , both \tilde{M}_{\max} and $\tilde{\omega}_{\min}$ increase monotonically with decreasing $\tilde{\Lambda}$.

Secondly, we confirmed that boson star frozen states characterized by $-g_{tt}(x \rightarrow x_c) \rightarrow 0$ still exist in AdS spacetime. The critical magnetic monopole charge \tilde{q}_c required to form frozen state solutions increases monotonically as $\tilde{\Lambda}$ decreases. These frozen states generate an effective hard boundary resembling a black hole event horizon, with the radius x_c of this boundary referred to as the critical horizon radius.

Further, we discussed the light rings (LRs) of boson stars, for which solutions exist for all values of \tilde{q} . As \tilde{q} increases, the distribution range of the light ring solutions on the \tilde{M} - $\tilde{\omega}$ curve transitions from partial regions to the entire curve. In the frozen state, there exists an inner stable light ring located within the critical horizon ($\tilde{r}_{\text{inner}}^{\text{LR}} < x_c$) and an outer unstable light ring outside the critical horizon ($\tilde{r}_{\text{outer}}^{\text{LR}} > x_c$). As $\tilde{\Lambda}$ decreases, the distance between these two rings increases, manifested by a decrease in the inner LR radius and an increase in the outer LR radius.

At last for accretion disks, we have demonstrated that the innermost stable circular orbit (ISCO) radius \tilde{r}_{ISCO} reaches its maximum value when $\tilde{\Lambda} = 0$, while the orbital energy E_{ISCO} and angular momentum L_{ISCO} monotonically increase as $\tilde{\Lambda}$ decreases. Ray tracing simulations show that the observable spectral distribution of the accretion disk and the image of shadow are significantly influenced by the $\tilde{\Lambda}$ parameter.

Finally, we found that the radius of the innermost stable circular orbit (ISCO) \tilde{r}_{ISCO} for particles moving in the accretion disk reaches its maximum when $\tilde{\Lambda} = 0$, while the orbital energy E_{ISCO} and angular momentum L_{ISCO} of the particles monotonically increase as $\tilde{\Lambda}$ decreases. Ray-tracing simulations indicate that: (1) Compared to a Schwarzschild

black hole, the shadow region of a boson star can contain a additional photon ring. (2) The observable spectral distribution on the accretion disk and the shadow image are significantly influenced by the cosmological constant $\tilde{\Lambda}$.

6 Acknowledgment

This work is supported by the National Natural Science Foundation of China (Grant No. 12275110 and No. 12247101) and the National Key Research and Development Program of China (Grant No. 2022YFC2204101 and 2020YFC2201503).

References

- [1] A. Einstein, *The foundation of the general theory of relativity.*, *Annalen Phys.* **49** (1916) 769.
- [2] K. Schwarzschild, *On the gravitational field of a mass point according to Einstein's theory*, *Sitzungsber. Preuss. Akad. Wiss. Berlin (Math. Phys.)* **1916** (1916) 189.
- [3] R. P. Kerr, *Gravitational field of a spinning mass as an example of algebraically special metrics*, *Physical Review Letters* **11** (1963) 237.
- [4] E. T. Newman, E. Couch, K. Chinnapared, A. Exton, A. Prakash and R. Torrence, *Metric of a Rotating, Charged Mass*, *Journal of Mathematical Physics* **6** (1965) 918.
- [5] M. F. Shirokov, *Solutions of the Schwarzschild-Nordstrom type for a point charge without singularities*, *Soviet Phys. JETP* **18** (1948) 236.
- [6] Y.-S. Duan, *Generalization of regular solutions of Einstein's gravity equations and Maxwell's equations for point-like charge*, *Soviet Physics JETP* **27** (1954) 756 [[1705.07752](#)].
- [7] A. D. Sakharov, *The Initial Stage of an Expanding Universe and the Appearance of a Nonuniform Distribution of Matter*, *Soviet Journal of Experimental and Theoretical Physics* **22** (1966) 241.
- [8] E. B. Gliner, *Algebraic Properties of the Energy-momentum Tensor and Vacuum-like States of Matter*, *Soviet Journal of Experimental and Theoretical Physics* **22** (1966) 378.
- [9] J. Bardeen in *Conference Proceedings*, (Tiflis, U.S.S.R.), 1968.
- [10] S. A. Hayward, *Formation and evaporation of non-singular black holes*, *Phys. Rev. Lett.* **96** (2006) 031103 [[gr-qc/0506126](#)].
- [11] E. Ayón-Beato and A. García, *Regular Black Hole in General Relativity Coupled to Nonlinear Electrodynamics*, *Physical Review Letters* **80** (1998) 5056 [[gr-qc/9911046](#)].
- [12] E. Ayón-Beato and A. García, *The Bardeen model as a nonlinear magnetic monopole*, *Physics Letters B* **493** (2000) 149 [[gr-qc/0009077](#)].
- [13] Z.-Y. Fan and X. Wang, *Construction of Regular Black Holes in General Relativity*, *Phys. Rev. D* **94** (2016) 124027 [[1610.02636](#)].
- [14] S. W. Hawking and D. N. Page, *Thermodynamics of black holes in anti-de Sitter space*, *Communications in Mathematical Physics* **87** (1983) 577.
- [15] Z.-Y. Fan, *Critical phenomena of regular black holes in anti-de Sitter space-time*, *Eur. Phys. J. C* **77** (2017) 266 [[1609.04489](#)].

- [16] A. Halder and R. Biswas, *Thermodynamic Studies of Different Black Holes with Modifications of Entropy*, *Astrophys. Space Sci.* **363** (2018) 27 [[1903.03430](#)].
- [17] S. Guo, J. Pu and Q.-Q. Jiang, *Joule-Thomson Expansion of Hayward-AdS black hole*, [1905.03604](#).
- [18] T. Takayanagi and K. Tamaoka, *Gravity Edges Modes and Hayward Term*, *JHEP* **02** (2020) 167 [[1912.01636](#)].
- [19] K. K. J. Rodrigue, M. Saleh, B. B. Thomas and T. C. Kofane, *Thermodynamic Phase Transition and global stability of the Regular Hayward Black hole Surrounded by Quintessence*, *Mod. Phys. Lett. A* **35** (2020) 2050129 [[1808.03474](#)].
- [20] A. N. Kumara, C. L. A. Rizwan, K. Hegde and A. K. M, *Repulsive Interactions in the Microstructure of Regular Hayward Black Hole in Anti-de Sitter Spacetime*, *Phys. Lett. B* **807** (2020) 135556 [[2003.10175](#)].
- [21] S. Guo, Y. L. Huang, K. J. He and G. P. Li, *Hayward black hole heat engine efficiency in anti-de Sitter space*, *Mod. Phys. Lett. A* **36** (2021) 2150108.
- [22] A. N. Kumara, C. L. A. Rizwan, K. Hegde, A. K. M and M. S. Ali, *Microstructure and continuous phase transition of a regular Hayward black hole in anti-de Sitter spacetime*, *PTEP* **2021** (2021) 073E01 [[2003.00889](#)].
- [23] M. Zhang, C.-M. Zhang, D.-C. Zou and R.-H. Yue, *P - V criticality and Joule-Thomson Expansion of Hayward-AdS black holes in 4D Einstein-Gauss-Bonnet gravity*, *Nucl. Phys. B* **973** (2021) 115608 [[2102.04308](#)].
- [24] S. Guo, Y.-L. Huang and E.-W. Liang, *Comparison of thermodynamic behaviors of two regular-AdS black holes*, *Commun. Theor. Phys.* **74** (2022) 025402 [[2009.03519](#)].
- [25] A. Belhaj, M. Benali, H. E. Moumni, M. A. Essebani, M. B. Sedra and Y. Sekhmani, *Thermodynamic and Optical Behaviors of Quintessential Hayward-AdS Black Holes*, *Int. J. Geom. Meth. Mod. Phys.* **19** (2022) 2250096 [[2202.06290](#)].
- [26] H. Iguchi, *Gravitational Entropy of Hayward Black Hole*, *Annals Phys.* **453** (2023) 169331 [[2504.10890](#)].
- [27] M. Rizwan and K. Jusufi, *Topological classes of thermodynamics of black holes in perfect fluid dark matter background*, *Eur. Phys. J. C* **83** (2023) 944 [[2310.15182](#)].
- [28] A. N. Kumara, S. Punacha, K. Hegde, C. L. A. Rizwan, M. S. Ali and K. M. Ajith, *Dynamics and kinetics of phase transition for regular AdS black holes in general relativity coupled to non-linear electrodynamics*, *Int. J. Mod. Phys. A* **38** (2023) 2350151 [[2106.11095](#)].
- [29] Y. Guo, H. Xie and Y.-G. Miao, *Signal of phase transition hidden in quasinormal modes of regular AdS black holes*, *Phys. Lett. B* **855** (2024) 138801 [[2402.10406](#)].
- [30] N. J. Gogoi, S. Acharjee and P. Phukon, *Lyapunov Exponents and Phase Transition of Hayward AdS Black Hole*, *Eur. Phys. J. C* **84** (2024) 1144 [[2404.03947](#)].
- [31] L.-B. Wu, R.-G. Cai and L. Xie, *The stability of the greybody factor of Hayward black hole*, *Phys. Rev. D* **111** (2025) 044066 [[2411.07734](#)].
- [32] F. F. Nascimento, V. B. Bezerra, J. M. Toledo and G. A. Marques, *Some remarks on Hayward-AdS black hole surrounded by a fluid of strings*, *Gen. Rel. Grav.* **56** (2024) 86 [[2412.00552](#)].

- [33] M. Cadoni, M. Oi and A. P. Sanna, *Effective models of non-singular quantum black holes*, *Phys. Rev. D* **106** (2022) 024030 [[2204.09444](#)].
- [34] B. Toshmatov, A. Abdujabbarov, Z. Stuchlík and B. Ahmedov, *Quasinormal modes of test fields around regular black holes*, *Phys. Rev. D* **91** (2015) 083008 [[1503.05737](#)].
- [35] O. Pedraza, L. A. López, R. Arceo and I. Cabrera-Munguia, *Quasinormal modes of the Hayward black hole surrounded by quintessence: Scalar, electromagnetic and gravitational perturbations*, *Mod. Phys. Lett. A* **37** (2022) 2250057 [[2111.06488](#)].
- [36] P. D. Roy and S. Kar, *Generalised Hayward spacetimes: Geometry, matter and scalar quasinormal modes*, *Phys. Rev. D* **106** (2022) 044028 [[2206.04505](#)].
- [37] D. Zhang, H. Gong, G. Fu, J.-P. Wu and Q. Pan, *Quasinormal modes of a regular black hole with sub-Planckian curvature*, *Eur. Phys. J. C* **84** (2024) 564 [[2402.15085](#)].
- [38] Z. Malik, *Analytical QNMs of fields of various spin in the Hayward spacetime*, *EPL* **147** (2024) 69001 [[2410.04306](#)].
- [39] X.-P. Rao and H. Huang, *Can we distinguish whether black holes have singularities or not through echoes and light rings?*, May, 2025. 10.48550/arXiv.2505.11073.
- [40] Z. Luo, H. Yu, S. Cao and J. Li, *Shadow thermodynamics of the Hayward-AdS black hole*, *Chin. Phys. C* **47** (2023) 065102 [[2301.06120](#)].
- [41] F. H. Vincent, Z. Meliani, P. Grandclément, E.ourgoulhon and O. Straub, *Imaging a boson star at the Galactic center*, *Class. Quant. Grav.* **33** (2016) 105015 [[1510.04170](#)].
- [42] P. V. P. Cunha, J. A. Font, C. Herdeiro, E. Radu, N. Sanchis-Gual and M. Zilhão, *Lensing and dynamics of ultracompact bosonic stars*, *Phys. Rev. D* **96** (2017) 104040 [[1709.06118](#)].
- [43] H. Olivares, Z. Younsi, C. M. Fromm, M. De Laurentis, O. Porth, Y. Mizuno et al., *How to tell an accreting boson star from a black hole*, *Mon. Not. Roy. Astron. Soc.* **497** (2020) 521 [[1809.08682](#)].
- [44] J. L. Rosa, P. Garcia, F. H. Vincent and V. Cardoso, *Observational signatures of hot spots orbiting horizonless objects*, *Phys. Rev. D* **106** (2022) 044031 [[2205.11541](#)].
- [45] J. L. Rosa and D. Rubiera-Garcia, *Shadows of boson and Proca stars with thin accretion disks*, *Physical Review D* **106** (2022) 084004 [[2204.12949](#)].
- [46] J. L. Rosa, C. F. B. Macedo and D. Rubiera-Garcia, *Imaging compact boson stars with hot-spots and thin accretion disks*, *Phys. Rev. D* **108** (2023) 044021 [[2303.17296](#)].
- [47] J. L. Rosa, J. Pelle and D. Pérez, *Accretion disks and relativistic line broadening in boson star spacetimes*, *Phys. Rev. D* **110** (2024) 084068 [[2403.11540](#)].
- [48] P. L. B. de Sá, H. C. D. Lima, C. A. R. Herdeiro and L. C. B. Crispino, *Static boson stars in the Einstein-Friedberg-Lee-Sirlin theory and their astrophysical images*, *Phys. Rev. D* **110** (2024) 104047 [[2406.02695](#)].
- [49] K. Gjorgjeski, J. Kunz and P. Nedkova, *Comparison of magnetized thick disks around black holes and boson stars*, *Eur. Phys. J. C* **84** (2024) 286 [[2401.13857](#)].
- [50] X.-X. Zeng, C.-Y. Yang, Y.-X. Huang, K.-J. He, G.-P. Li and S. Guo, *Optical Images of Mini Boson Stars in Palatini $f(R)$ Gravity*, [2501.13764](#).
- [51] G.-P. Li, M.-Q. Wu, K.-J. He and Q.-Q. Jiang, *Observational features of massive boson stars with thin disk accretion*, [2505.14734](#).

- [52] K.-J. He, G.-P. Li, C.-Y. Yang and X.-X. Zeng, *The observation image of a soliton boson star illuminated by various accretions*, [2502.16623](#).
- [53] Y. Huang, D.-J. Liu and H. Zhang, *Lensing and light rings of parity-odd rotating boson stars*, *Sci. China Phys. Mech. Astron.* **68** (2025) 280411 [[2410.20867](#)].
- [54] R. Ruffini and S. Bonazzola, *Systems of selfgravitating particles in general relativity and the concept of an equation of state*, *Phys. Rev.* **187** (1969) 1767.
- [55] D. Astefanesei and E. Radu, *Boson stars with negative cosmological constant*, *Nucl. Phys. B* **665** (2003) 594 [[gr-qc/0309131](#)].
- [56] B. Hartmann and J. Riedel, *Supersymmetric Q-balls and boson stars in $(d+1)$ dimensions*, *Phys. Rev. D* **87** (2013) 044003 [[1210.0096](#)].
- [57] Y. Brihaye, B. Hartmann and J. Riedel, *Self-interacting boson stars with a single Killing vector field in Anti-de Sitter*, *Phys. Rev. D* **92** (2015) 044049 [[1404.1874](#)].
- [58] Y. Brihaye, F. Console and B. Hartmann, *Charged and radially excited boson stars (in Anti-de Sitter)*, *Phys. Rev. D* **106** (2022) 104058 [[2209.07978](#)].
- [59] X.-Y. Zhang, L. Zhao and Y.-Q. Wang, *Dirac stars in Anti-de Sitter spacetime*, *Eur. Phys. J. C* **84** (2024) 954 [[2401.04547](#)].
- [60] X.-Y. Zhang, L. Zhao and Y.-Q. Wang, *Bardeen-Dirac Stars in AdS Spacetime*, *JCAP* **01** (2025) 117 [[2409.14402](#)].
- [61] M. Duarte and R. Brito, *Asymptotically anti-de Sitter Proca Stars*, *Phys. Rev. D* **94** (2016) 064055 [[1609.01735](#)].
- [62] Y. Yue and Y.-Q. Wang, *Frozen Hayward-boson stars*, [2312.07224](#).
- [63] I. A. Baratta, J. P. Dean, J. S. Dokken, M. Habera, J. S. Hale, C. N. Richardson et al., *DOLFINx: The next generation FEniCS problem solving environment*, Dec., 2023. 10.5281/zenodo.10447666.
- [64] M. W. Scroggs, J. S. Dokken, C. N. Richardson and G. N. Wells, *Construction of arbitrary order finite element degree-of-freedom maps on polygonal and polyhedral cell meshes*, *ACM Transactions on Mathematical Software* **48** (2022) 18:1.
- [65] M. W. Scroggs, I. A. Baratta, C. N. Richardson and G. N. Wells, *Basix: A runtime finite element basis evaluation library*, *Journal of Open Source Software* **7** (2022) 3982.
- [66] M. S. Alnaes, A. Logg, K. B. Ølgaard, M. E. Rognes and G. N. Wells, *Unified Form Language: A domain-specific language for weak formulations of partial differential equations*, *ACM Transactions on Mathematical Software* **40** (2014) .
- [67] Ya. B. Zeldovich and I. D. Novikov, *Stars and Relativity*, vol. 1 of *Relativistic Astrophysics*. University of Chicago Press, Chicago, translation from the 1967 russian edition ed., 1971.
- [68] L.-X. Huang, S.-X. Sun and Y.-Q. Wang, *Frozen Bardeen-Dirac stars and light ball*, *Eur. Phys. J. C* **85** (2025) 357 [[2312.07400](#)].
- [69] J.-R. Chen and Y.-Q. Wang, *Hayward spacetime with axion scalar field*, [2407.17278](#).
- [70] P. V. P. Cunha, E. Berti and C. A. R. Herdeiro, *Light ring stability in ultra-compact objects*, *Physical Review Letters* **119** (2017) 251102 [[1708.04211](#)].
- [71] C. F. B. Macedo, P. Pani, V. Cardoso and L. C. B. Crispino, *Astrophysical signatures of*

- boson stars: Quasinormal modes and inspiral resonances*, *Phys. Rev. D* **88** (2013) 064046 [[1307.4812](#)].
- [72] J. P. Luminet, *Image of a spherical black hole with thin accretion disk.*, *Astronomy and Astrophysics* **75** (1979) 228.
 - [73] I. D. Novikov and K. S. Thorne, *Astrophysics of black holes*, in *Black Holes*, Edited by C. DeWitt and B. DeWitt, pp. 343–450. Gordon and Breach, New York, 1973.
 - [74] D. N. Page and K. S. Thorne, *Disk-Accretion onto a Black Hole. Time-Averaged Structure of Accretion Disk*, *Astrophys. J.* **191** (1974) 499.
 - [75] EVENT HORIZON TELESCOPE collaboration, K. Akiyama, A. Alberdi, W. Alef et al., *First M87 Event Horizon Telescope Results. I. The Shadow of the Supermassive Black Hole*, *Astrophys. J. Lett.* **875** (2019) L1 [[1906.11238](#)].
 - [76] EVENT HORIZON TELESCOPE collaboration, A. W. Raymond, S. S. Doeleman, K. Asada, L. Blackburn, G. C. Bower, M. Bremer et al., *First Very Long Baseline Interferometry Detections at 870 Mm*, *Astron. J.* **168** (2024) 130 [[2410.07453](#)].
 - [77] G. Gyulchev, P. Nedkova, T. Vetsov and S. Yazadjiev, *Image of the thin accretion disk around compact objects in the Einstein–Gauss–Bonnet gravity*, *Eur. Phys. J. C* **81** (2021) 885 [[2106.14697](#)].
 - [78] O. Y. Tsupko, *Shape of higher-order images of equatorial emission rings around a Schwarzschild black hole: Analytical description with polar curves*, *Phys. Rev. D* **106** (2022) 064033 [[2208.02084](#)].
 - [79] G. J. Olmo, D. Rubiera-Garcia and D. Sáez-Chillón Gómez, *New light rings from multiple critical curves as observational signatures of black hole mimickers*, *Phys. Lett. B* **829** (2022) 137045 [[2110.10002](#)].
 - [80] J. L. Rosa, *Observational properties of relativistic fluid spheres with thin accretion disks*, *Phys. Rev. D* **107** (2023) 084048 [[2302.11915](#)].
 - [81] Y.-X. Gao, *Higher-order photon rings of an ultracompact object and their interferometric pattern*, **2504.16719**.